PROCESSING AND MECHANICAL CHARACTERIZATION OF
HYBRID Al-Ti-Ta MATRIX COMPOSITE

By

IN HWAN HWANG

A DISSERTATION PRESENTED TO THE GRADUATE SCHOOL
OF THE UNIVERSITY OF FLORIDA IN PARTIAL FULFILLMENT
OF THE REQUIREMENTS FOR THE DEGREE OF
DOCTOR OF PHILOSOPHY

UNIVERSITY OF FLORIDA

1996

ACKNOWLEDGEMENTS

I would like to express my deep gratitude to my dissertation advisor and committee chair, Dr. Reza Abbaschian, for his sincere guidance, suggestions, and support throughout the course of the study and dissertation work. I feel honored to have known and been helped by such a nice person. I am also indebted to Dr. Robert T. DeHoff, Dr. Fereshteh Ebrahimi, Dr. Michael J. Kaufman, and Dr. Bhavani V. Sankar for serving on my Supervisory Committee and for reviewing and suggesting improvements in this study.

I would like to thank colleagues of the Metal Processing Group for beneficial discussions and pleasant times we shared. Special thanks go to Lu, Xiao and Atul.

Special thanks are given to Dr. Sunmoo Hur, Mr. Yongjin Lim, and other Gainesville friends for help and encouragement to finish this once-interrupted work.

I am deeply indebted to my family for love, consistent support and encouragement throughout my entire life, including my parents and eldest brother, In Kwang. I cannot forget my children, Juha and Shinha who sacrificed so much during this time. Last, but first in my heart, I thank my wife, Moonju for her continuous support, understanding and love. I am especially grateful for her presence and help when I need it.

TABLE OF CONTENTS

PROCESSING AND MECHANICAL CHARACTERIZATION OF
HYBRID Al-Ti-Ta MATRIX COMPOSITE

By

In Hwan Hwang

December 1996

Chairperson: Dr. R. Abbaschian
Major Department: Materials Science and Engineering

In this study, dual reinforced composites based on Al-
25at.%Ti-25at.%Ta intermetallic were designed and implemented
through synthesis and analysis to obtain preferred mechanical
properties at ambient as well as elevated temperatures.
Interfacial properties and the role of ductile metallic fibers
and hard ceramic fibers in the composites were analyzed. The
composites were reinforced with discontinuous alumina fibers
and/or niobium fibers to improve high-temperature strength and
stiffness and ambient temperature fracture toughness of the
matrix. Mechanical properties and microstructure of the
composites were analyzed by testing the materials at room and
elevated temperatures of 1273 and 1473 K. The mechanical
behavior of the composites was investigated by four-point
flexural testing. It was found that the fracture toughness of
the composites reinforced with short niobium fibers, as

determined by four-point flexural testing of chevron-notched beam specimens, was improved over that of the unreinforced matrix material at room temperature. Toughness improvement also was found to be a function of the volume fraction of fibers. Loading of short alumina fibers, on the other hand, toughened the matrix material only slightly due to strong interfacial bonds and lack of fiber pullout mechanism.

Increased stiffness and strength at room and high temperatures of 1273 and 1473 K were observed in composites reinforced with short alumina fibers compared to the unreinforced alloy. The elastic modulus of the composites changed linearly with increase of fiber volume fraction but less than the values expected by the rule of mixtures. The four-point flexural strength also varied with increasing fiber volume fraction.

Hybrid composites were synthesized with short alumina and niobium fibers. The hybrid composites compensated for drawbacks when one kind of fibers was applied, and they achieved simultaneous enhancement in strength/modulus at high tempertures and also togheness at room temperature.

CHAPTER ONE
INTRODUCTION

The development of an advanced aerospace system such as high-performance gas turbine engines demands the introduction of new materials, which can be used above the temperatures where the existing materials can withstand the harsh environment. Intermetallic compounds are currently considered potential materials for these applications because of their relatively good high-temperature properties (e.g., combination of strength, stiffness, and resistance to creep and oxidation). However, intermetallics possess limited capabilities as high-temperature structural materials because of lack of low-temperature ductility and toughness and of limited high-temperature strength.

Various attempts have been made to improve properties of intermetallics by dispersing ductile phase particles, dispersing oxide-forming rare earth metals, or adding an intermetallic compound-forming metalloid. The most effective way to improve low- and high-temperature mechanical properties of intermetallics might be to fabricate intermetallic composites reinforced with fibers and/or sheets.

The alloy with a composition of Al-25at.%Ti-25at.%Ta[1] has attractive properties for application in aircraft services as components of propulsion systems and advanced airframes. However, the two-phase intermetallic alloy showed low toughness at ambient temperature [Dev91] and required higher strength and stiffness at high temperatures [Ale89, Alm91]. For the current knowledge in composites, simultaneous achievement in high levels of toughness and strength is very hard. Enhancement of one results in deterioration of the other. Thus, development of materials for high-temperature applications is necessary to achieve the combined goal of increased room-temperature toughness plus high-temperature strength. The improvement in properties of this kind of prospective materials by compositing should be correlated with microstructural parameters so as to contribute to a better understanding of the material performance and give a guidance for further improvement in properties in the composite group.

In this study, the research goals were as follows: (a) demonstrate the chemical stability of reinforcements in the composites at high temperatures, (b) develop a processing technique and optimize processing parameters to synthesize dual-fiber reinforced composites using short ductile and hard fibers, and (c) modify the properties of the alloy by compositing to improve toughness of the material at room

---

[1] The alloy compositions in this study are expressed in atomic percentage unless noted otherwise.

temperature, and also to enhance high-temperature strength and stiffness. Effect of loading simultaneously two kinds of fibers with the different properties into a composite was analyzed to optimize the properties of composites.

Al-Ti-Ta Ternary Alloys

Al-Ti-Ta Phase Diagram

Revived interest in intermetallics for possible applications at high temperatures has promoted extensive investigation into phase equilibria in the Al-Ti-Ta ternary system in recent years. Recent revisions to the binary Al-Ti phase diagram [Mcc89, Mur86] and re-evaluation of the Al-Ta binary system [Sub90] also have necessitated extensive revision of the ternary phase diagram. Das and Perepezko [Das91a, Das91b] re-examined the ternary phase diagrams of Raman [Ram66] and of Sridharan and Nowotny [Sri83]. They confirmed most of their work but noted a shift in boundaries between equilibrium phases. Perepezko and his coworker [Das91b] investigated high-temperature phase equilibria in diffusion couples and suggested a revised isothermal section of the Al-Ti-Ta system at 1373 K that involved more extensive solubility of Ta in γ-TiAl, extended the η-(Ti,Ta)Al$_3$ field, and included a new Ti$_2$TaAl phase.

An isothermal section of a recently suggested phase diagram of the Al-Ti-Ta ternary system is shown in Figure 2.1

[Das91a, Dev91]. The phase diagram includes the following phases: (1) the fcc Al solid solution; (2) the continuous solid solution between Ta and Ti (ß) with a bcc structure; (3) the hcp Ti solid solution (α); (4) an ordered hexagonal DO_{19} structure based on the α structure (α_2-Ti_3Al); (5) an ordered $L1_0$ fct phase (γ-TiAl); (6) the continuous solid solution between $TiAl_3$ and $TaAl_3$ (η) with a DO_{22} ordered fcc structure; (7) an ordered $D8_b$ structure (σ-Ta_2Al); and (8) an ordered bcc B2 ternary phase near the composition of Ti_2TaAl, represented as "T" in the phase diagram.

McCullough et al. [Mcc91] investigated high-temperature phase equilibria during solidification of the ternary alloys and drew a similar isothermal section at 1373 K. They found that in alloys with Al contents of 48-56%, the primary α-(Ti) formed with γ as segregate from the melt. Alloys with higher Ta contents (>10%) in combination with Al contents lower than 50% solidified with the primary phase of ß-(Ti,Ta) solid solution surrounded by peritectic α and γ segregates, as in the equivalent Al-Ti alloys (45-48% Al). Significant coring with Ta enrichment at the dendrite cores was found to transform to σ and ultimately to form a lamellar (σ+γ) microstructure during cooling. At lower Ta contents the dendrite bulk regions were dominated by the decomposition of α to the (α_2+γ) lath; however, with increasing Ta levels, these were replaced by polycrystalline γ and σ precipitation.
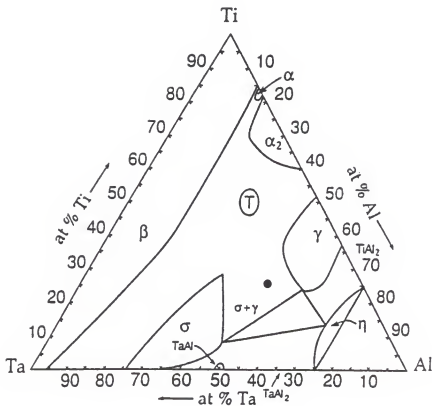
Figure 2.1 Isothermal section at 1473 K of the Al-Ti-Ta ternary system from [Dev91].

Boettinger et al. [Boe91] determined the stable phases at temperatures between 1473 and 1823 K. They suggested a partial isothermal section at 1603 K that includes two three-phase fields, $\alpha+\beta+\sigma$ and $\alpha+\gamma+\sigma$ in alloys with composition close to Al-25%Ti-25%Ta. The alloy consisted of $\gamma+\sigma$ below 1598 K and transformed to various multiphase structures composed of σ, α, and β during heating between 1598 and 1698 K. The alloy transformed further to two phases, $\alpha+\beta$, between 1698 and 1773 K and to a single phase, β, between 1798 and 1823 K.

Weaver and his co-workers [Wea91, Wea92] determined the phase transformation and equilibria in the ternary alloy system and constructed isothermal sections at 1623 and 1723 K. They found that the $\alpha+\beta$ field existed near the composition Al-25%Ti-25%Ta at 1723 K and the $\alpha+\sigma$ region existed below 1672 K. They indicated the existence of δ phase at 1723 K. Further investigation [Boe91] showed that the alloy transforms to multiphase structures composed of σ, α, and β above 1598 K, and to two phase $\alpha+\beta$ above 1698 K; between 1798 and 1823 K the alloy is β phase.

A ternary phase with ordered bcc, B2 (CsCl type) structure at high temperatures analogue to Ti_2NbAl found in Al-Ti-Nb system has been reported [Kim89, Per90]. Das and Perepezko [Das91b] also found the new ternary phase near the composition of Ti_2TaAl at 1373 K in an annealed diffusion couple. Weaver et al. [Wea91] confirmed the existence of the phase in some alloys of the ternary system after examination

of samples quenched from 1723 K by room temperature XRD and TEM.

McCullough et al. [Mcc91] and Boettinger et al. [Boe91] examined phase equilibria at high temperatures in an alloy of Al-25%Ti-25%Ta and reported that the alloy consisted only of gamma and sigma phases below 1598 K. Kim et al. [Kim89] found that the alloys around Al-25%Ti-25%Ta contain two phases, γ and σ. The Al-25%Ti-25%Ta alloy used in this study has a two-phase microstructure.

Properties of Al-Ti-Ta Alloys

Information on properties of the matrix materials is requisite to development of new composite materials based on the matrix. However, Al-Ti-Ta alloys have attracted attention recently, and their physical and chemical properties are not well known. A review on properties of other intermetallic systems close to the Al-Ti-Ta alloys is given here in order to understand the properties of the material.

Titanium aluminides based on the compositions Ti_3Al and TiAl are of interest as aerospace structural materials due to their light weight, as well as relatively good properties and oxidation resistance at high temperatures. Most of the intermetallics like titanium aluminides have high melting temperatures because they have complex, low-symmetry crystal structures that have strong directional atomic bonds. It is generally believed that strong bonding is responsible for

retention of mechanical properties, such as high strength, stiffness, and creep resistance (due to high activation energy required for diffusion) up to very high temperatures, and data on the materials have shown that these properties are proportional to their melting points.

The intermetallics are hard and brittle because they have strong directional atomic bonds and there are very few slip systems available in the materials when compared to metals. Thus, the common fracture mode is slip-induced cracking by either grain-boundary decohesion or cracking along planar slip bands in Ti-Al alloys with $\gamma + \alpha_2$ microstructure [Lip75, Cha92]. These result in characteristically low failure strains and low toughness or fracture energy. Besides being brittle, they have low tensile strengths. The deformation characters of the aluminides can be changed by the alteration of microstructure or alloy composition. The microstructure can be controlled by changing the composition and thermomechanical history of the alloy. For example, in titanium aluminide alloys based on γ-TiAl, three main microstructures have been observed: equiaxed γ grains, sometimes with small amounts of α_2 particles at grain boundaries; lamellar structure comprised of alternating layers of α_2 and γ platelets; and duplex microstructure consisting of a mixture of γ grains and γ/α_2 lamellar colonies. The relative amounts and distribution of these constituting morphologies are the main factors

controlling mechanical properties, such as strength, ductility and fracture toughness of the alloys.

Although their mechanical properties at high temperatures are better than superalloys currently used, the high-temperature capabilities of TiAl and Ti$_3$Al are considered to be limited to about 1150 and 1030 K, respectively, due to oxidation when not coated [Lip85]. In addition, titanium aluminides have insufficient creep strengths for high temperature structural applications.

Alloying elements such as niobium and tantalum can be added in significant amounts to increase ambient-temperature toughness and high-temperature properties of γ-TiAl. Tantalum is attractive due to its higher melting point and better oxidation resistance than niobium even though niobium's density is higher. Particularly, alloys based on the composition of Al-25%Ti-25%Ta are currently of interest in the development of a new class of high-temperature materials due to their increased oxidation resistance and solidus temperature over Al-Ti or Al-Ti-Nb alloys [Ale89]. At elevated temperatures the alloys based on Al-25%Ti-25%Ta form protective alumina scales that make them suitable for use in oxidizing environments.

The alloy is known to have a ductile-to-brittle transition temperatures (DBTT) in the range of 1123 to 1273 K, and its strength and creep resistance are better than those of the analogous ternary alloy Al-25%Ti-25%Nb [Cou89]. Both γ-

TiAl and σ-Ta$_2$Al have good mechanical properties at high temperatures due to strong atomic bonds, which also contribute to the lack of ductility and low fracture toughness of other intermetallics at ambient temperature. γ-TiAl shows a ductile-to-brittle transition near 973 K [Fle89, Lip75]. DBTT of σ-Ta$_2$Al is not known but expected to be higher, as suggested by DBTT of the analogous phase Nb$_2$Al, which is higher than 1423 K [Fle89]. With such a high ductile-to-brittle transition temperature, the σ phase also acts like a non-deforming reinforcement phase in the two-phase alloys at low temperature.

Design of Intermetallic Matrix Composites

Without sacrificing the desirable behavior of the intermetallics, improvement of their poor properties is important for the development of the intermetallics aerospace structural applications. These materials with high-melting points can be applied for high-temperature structural use, provided their low-temperature fracture-resistance can be improved without sacrificing their attractive high-temperature properties.

The microstructure and properties of the intermetallic alloy can be modified by alloying or heat treatment of the materials, including precipitation hardening, dispersion hardening, grain size control, and forming a dual-phase microstructure. Ebrahimi et al. [Ebr93, Ebr95] studied

deformation of Al-Ti-Nb alloys with σ + γ phases at room and high temperatures and correlated it with heat treatment of the alloys. However, for high-temperature applications, compositing by incorporation of a discrete reinforcement phase (e.g., particles, whiskers, chopped fibers, or platelets) is considered a highly effective route to improve their properties. The stiffness can be improved by incorporating high-modulus fibers in a matrix but may reduce toughness of the matrix. A ductile reinforcement can toughen the intermetallic material, but it may reduce the modulus and also high temperature capability. Under consideration of high-temperature applications, chemical compatibility and difference in thermal expansion coefficients are additional factors that must be emphasized in selection of a suitable reinforcement material for the given matrix. The issue of which reinforcing material will be ultimately used to obtain the optimum mechanical properties in intermetallic composites remains unsolved.

Chemical Compatibility

Excessive chemical reactions lead to the deterioration of mechanical properties of composites. Interactions between matrix and reinforcements of composites may cause major changes in reinforcement, interface, and matrix. Possible deleterious interactions between constituting phases include chemical reaction between the matrix and reinforcement,

dissolution of the reinforcement into the matrix or the matrix into the reinforcement, phase change in the reinforcement, and change in the composition of matrix near the interface zone.

Thermodynamic considerations for interactions between the reinforcement and matrix at high temperatures provide predictions of possible interactions and a starting point for the selecting the reinforcements or coatings for high-temperature composites. However, accurate thermodynamic data often are lacking for such consideration. Interaction also may involve several alternative reaction routes such as intermediate phase formation, ternary or higher-order compound formation, and spinel formation. Information about some of these routes can be identified by examining phase diagrams if available, whereas others have to be determined by experiments. Also, reaction kinetics must be evaluated in the predicted reactive systems because some composites can be thermodynamically unstable but kinetically stable.

In this study, chemical compatibility between the AlTiTa alloy and preselected reinforcement materials in composites is reported. Evaluation of the reinforcements and diffusion barrier coatings was limited to those ceramics which are available in the commercial market in the form of oxides, carbides, nitrides, and other refractory compounds. Among refractory metals, niobium also was evaluated because pure niobium is ductile and available in the form of foils or small-diameter wires. The approach based on fundamental

thermodynamic principles was used to decide whether a reaction in the given system is thermodynamically favorable or not. If a reaction is thermodynamically feasible, then kinetic factors may decide the extent of the reaction and actual process behavior.

Physical Compatibility

One of the most important factors in design of composites is the difference coefficient of thermal expansion (CTE) of the reinforcement, α_f, and of the matrix, α_m. Generally, composite fabrication temperature is so high that the matrix material deforms significantly by plastic deformation. However, upon cooling from the processing temperature, a thermal strain mismatch between the reinforcement and matrix is developed which is nearly proportional to the CTE mismatch and temperature change. If the reinforcement contracts more than the matrix, then the reinforcement will be subjected to a residual tensile stress and the matrix to a residual compressive stress, and vice versa. A detailed quantitative view of thermal stresses is discussed in the section on Effect of Thermal Residual Stress in this chapter. In practice, α_f and α_m must be kept close, but, if not, the condition $\alpha_f > \alpha_m$ is preferable to the reverse when the reinforcement is more capable of withstanding tensile strains than the intermetallic matrix.

Mechanical Properties of Composites

Several analytical composite models have been formulated to predict mechanical properties of composites based on the properties of the constituent phases (i.e., matrix and reinforcement). Some of these are briefly reviewed as follows and considered in the application of short fibers to composites.

For a composite where reinforcing phases are uniform, continuous, and unidirectionally distributed, the simple rule of mixtures (ROM) can be applied to predict some of their mechanical properties. When a stress is applied along its longitudinal direction, and a good bond is maintained between the matrix and the reinforcements so that no slip can occur at the interfaces, the externally applied shear strain is equal to the shear strain in all the composite phases including the matrix. The composite shear modulus is approximated by

$$\mu_c = \sum_{i=0}^{n} V_i \mu_i \qquad (2.1)$$

where

$$\sum_{i=0}^{n} V_i = 1 \qquad (2.2)$$

and the matrix has a shear modulus μ_0 and a volume fraction V_0,

and the corresponding values of shear moduli and volume fractions μ_i and V_i (where i = 1, 2, ..., n) for n different reinforcing phases, respectively. Because of its simplicity, the eq. (2.1) has been extended to predict other properties of composites, P_c, such as strength, elastic modulus, density, thermal expansion coefficient, and thermal conductivity.

$$P_c = \sum_{i=0}^{n} V_i P_i \tag{2.3}$$

In this study, the linear relationship commonly is called the rule of mixtures. For example, when the property of the composite is the Young's modulus, we can predict the Young's modulus of the composite E_c is given as

$$E_c = V_0 E_0 + V_1 E_1 + \cdots \tag{2.4}$$

where E_0 is Young's modulus of the matrix and E_i is that of the i th phase. The model is considered accurate in predicting the longitudinal modulus of elasticity of continuous fiber-reinforced composites [Hil52, Mcd65]. The model is also reasonably accurate for composites reinforced with aligned discontinuous fibers. Nevertheless, it should be noted that the value predicted by the simple rule of mixtures is an upper-bound approximation of the modulus because the strains

in the matrix and the reinforcements of a real composite are not the same.

The longitudinal moduli of composites with misoriented short fibers and the transverse moduli of composites with continuous or short fibers are far below the value predicted by the ROM estimation. When a stress is applied in the transverse direction of a unidirectional composite, it is carried by the matrix and the reinforcement in series. If the stress is assumed to be uniform throughout the composite and the total displacement in the thickness direction is the sum of displacements of the constituents, then, according to Reuss [Reu29], the composite strain is approximated as

$$\varepsilon_c = \sum_{i=0}^{n} \varepsilon_i V_i \qquad (2.5)$$

where ε_c is the composite strain in the transverse direction and ε_i is the strain in the ith phase. By considering the isostress condition, the Young's modulus of the composite, E_c is given by

$$\frac{1}{E_c} = \sum_{i=0}^{n} \frac{V_i}{E_i}. \qquad (2.6)$$

The two models given above are derived independently of the arrangement of the reinforcements or their shapes in the composite. Contributions from the interaction between the constituents or the interface between the matrix and reinforcement are also neglected. The assumption of uniform stress or strain also imposes restrictions on the geometrical arrangement of the constituents. However, in a real situation, strain or stress is not uniform. Therefore, the actual values of the mechanical properties lie between the linear relationship and Reuss estimations, which provide the upper and lower bounds of the properties.

Effect of Discontinuous Fibers

Deformation and load-bearing mechanism of composites is the transfer of loads between fibers and matrix and the resulting load distribution. Load transfer between discontinuous fibers and matrix is the action of shear strains and corresponding stresses in the matrix on planes and in directions parallel to the fibers. The fiber ends can not support the same load as the middle of the fiber. Hence, the rule of mixtures should be modified for composites reinforced with discontinuous fibers. Estimation of properties of composites with aligned short fibers was proposed based on the shear-lag analysis in a model composite [Kel64, Kel65a, Kel65b]. When a perfect bond between the matrix and fiber is assumed, the difference in longitudinal strains creates a

shear stress distribution across the interface. As shown in Figure 2.2, the stress on the fiber is zero at its ends and builds up to the maximum value at the central portion of the fiber for this idealized composite. Assuming no stress transfers at the fiber ends, the average stress on the fiber over a portion, l_c, of its length is, $\beta\sigma_f{}^u$, as shown in Figures 2.2 (a) and (b). When the fiber length exceeds l_c, the average stress, $\overline{\sigma}_f$, in the discontinuous fiber in Figure 2.2(c) can be given by

$$\overline{\sigma}_f = \frac{1}{l_f}\int_0^{l_f}\sigma_f\,dl = \frac{1}{l_f}[\sigma_f^u(l_f-l_c)+\beta\sigma_f^u l_c] \qquad (2.7)$$

or

$$\overline{\sigma}_f = \sigma_f^u[1-(1-\beta)\frac{l_c}{l_f}] \qquad (2.8)$$

where l_f is fiber length, σ_f is longitudinal stress applied to the fiber, and $\sigma_f{}^u$ is ultimate fiber strength. β is a load transfer function. with a value of 0.5 for an ideally plastic material; that is, the variation over the portion $l_c/2$ will be linear. This gives

$$\overline{\sigma}_f = \frac{l_f}{2l_c}\sigma_f^u \qquad (2.9)$$

for $l_f < l_c$, and

$$\overline{\sigma}_f = (1 - \frac{l_c}{2l_f}) \sigma_f^u \qquad (2.10)$$

for $l_f \geq l_c$. The critical length, l_c, is defined as the minimum fiber length required for the fiber stress to be equal to the ultimate fiber strength at its midlength, and expressed by

$$l_c = \frac{\sigma_f^u}{2\tau_i} d_f \qquad (2.11)$$

where d_f is the fiber diameter and τ_i is the interfacial shear strength but is substituted with the shear strength of the matrix when matrix failure starts before interfacial failure.

When the fiber-end effect is taken into account, the longitudinal strength of the composite, σ_c, is expressed according to the rule of mixtures as

$$\sigma_c = \overline{\sigma}_f V_f + \sigma_m V_m. \qquad (2.12)$$

For the case of $l_f \geq l_c$, the strength of the composite is calculated from eqs. 2.10 and 2.12 as

$$\sigma_c = (1 - \frac{l_c}{2l_f}) \sigma_f^u V_f + \sigma_m V_m. \qquad (2.13)$$
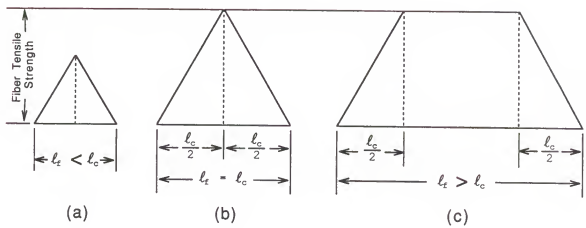
Figure 2.2 Significance of critical fiber length, l_c, on the longitudinal stresses of short fibers with length, (a) shorter than; (b) equal to; (c) longer than l_c.

For this case, the fiber fracture occurs when the average stress in the fibers reaches the stress for fiber fracture, provided that the fiber failure strain is lower than that of the matrix.

For shorter fibers ($l_f \langle l_c$), the longitudinal strength of the composite is given by eqs. 2.9, 2.11, and 2.12 as

$$\sigma_c = \frac{l_f}{d_f} \tau_i V_f + \sigma_m V_m. \qquad (2.14)$$

For these composites, two failure modes are possible before fibers start to fail: 1) interfacial bond failure and fiber pullout from the matrix and 2) matrix failure. When debonding and interfacial failure occur, τ_i is the shear strength of the fiber/matrix interface and σ_m is matrix stress at the instance of fiber failure. When matrix failure occurs initially, σ_m is tensile strength of the matrix material.

The expressions of the longitudinal stress of the composite with discontinuous fibers given by eqs. 2.13 and 2.14 can be generalized as

$$\sigma_c = \eta_L \sigma_f^u V_f + \sigma_m V_m \qquad (2.15)$$

where η_L is the length correction parameter of short fibers. Similarly, the shear-lag analysis derives the average axial stress in the fibers in conjunction with the rule of mixtures

[Kel73], and Young's modulus can be calculated as

$$E_c = \eta E_f V_f + E_m V_m \qquad (2.16)$$

The influence of fiber length on the average fiber strength contributed to the composite strength is shown in Figure 2.3. This shows that discontinuous fibers always strengthen a matrix to a lesser degree than continuous fibers. However, approximately 90% strengthening effect can be achieved with discontinuous fibers when fiber length exceeds five times the critical length, as an example. When the interfacial shear strength is so large that the critical length of the short fiber, l_c, becomes less than d_f (see equation 2.11), short fibers contribute to load transfer similar to continuous fibers.

Toughening of Composites

Fracture Toughness

Toughness of a material is the resistance to rapid crack propagation, or absence of brittleness, and usually measured by the amount of work absorbed before fracture. Toughness as a parameter of fracture resistance may be the area under a standard tension stress-strain curve taken to fracture, but is measured ordinarily on notched or pre-cracked specimens commonly under high-strain-rate loading conditions, such as an impact test. The bulk of investigations addressing the
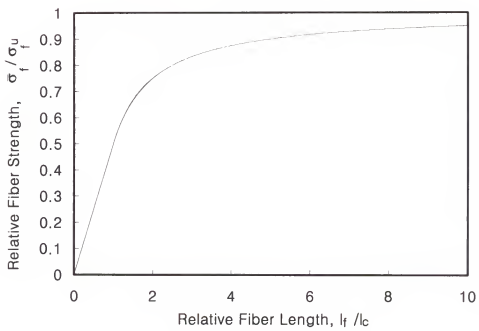
Figure 2.3   Variation in the longitudinal strength of an
aligned short fiber composite as a function of
fiber length.

toughness problem has focused mainly upon metallic materials. The metals exhibit a level of ductility in the fracturing process and are identified with relatively high toughness levels. Brittle materials, for which cracks start from defects and grow catastrophically, show low toughness levels. Thus, the concepts used for measuring toughness of homogeneous ceramics, such as linear fracture techniques and work of fracture measurements are valid for short fiber composites, provided most of the damage during fracture occurs close to a macroscopic fracture surface [Phi86]. The fracture toughness based on linear elastic fracture mechanisms has been successfully applied to short fiber metal matrix composites [Mcd85, Tay89].

Toughening Mechanisms in Composites

The microstructural aspects of toughening and fracture mechanics have been studied on numerous conventional metallic materials, and composites based on polymers(PMC), metals(MMC), and ceramics(CMC). Considering the brittleness of intermetallics, fracture mechanisms in intermetallic compound matrix composites(IMC) are similar to those applied to brittle ceramic or polymer matrix composites, although other properties of intermetallics like conductivities and chemical properties are comparable to metallic materials. The crack-tip behavior in intermetallics is substantially different from that observed in metals. The wake zone behind a crack tip in

the brittle phases controls the fracture behavior, whereas in the case of metals the plastic zone ahead of a crack tip is important.

Numerous mechanisms have been proposed to account for the observed toughening in brittle composites based on the initiation sources of their cracks including processing zone mechanisms and bridging zone mechanisms. Microstructural sources of toughening of process zone mechanisms are transformation and microcracking. Bridging zone mechanisms, on the other hand, are based on the toughening sources such as crack bridging by ductile phase reinforcements, brittle fibers or whiskers, and metallic binder networks. In other respects, fracture mechanisms in brittle composites can be grouped based on the following crack growth characteristics: crack-tip blunting by a ductile phase, crack shielding, crack deflection, crack bridging, crack branching, crack bowing, crack path tortuosity, crack pinning, and shear ligament toughening. In most cases, cracks grow frequently in a composite by a combination of several mechanisms. Some of the fracture mechanisms observed frequently in brittle matrix composite systems will be discussed briefly for understanding of failure in intermetallic composites.

Crack deflection

When a crack propagates, the crack plane can be reoriented away from normal to the applied tension by residual stress fields, grain boundaries, or fracture-resistant second

phase particles. Deviation from the original crack path causes a reduction in the local stress intensity factor and an increase in fracture toughness. The crack deflection occurs as the crack plane tilts about an axis parallel to the crack front or twists about an axis normal to the crack front. Faber and Evans [Fab83a] have shown that increased fracture toughness is contributed mostly by the twisting component of the crack plane. The prediction of the crack deflection model has been correlated with experimental measurements of toughening and crack deflection angles in Si_3N_4 and a glass ceramic [Fab83b] and in SiC [Fab83c]. These results suggest that the toughening derived from randomly oriented, deflecting particles depends only on the volume fraction and shape of the particles. Rod-shaped particles with large aspect ratio impart maximum toughening because of their influence on twist angle. An important characteristic of this model is its independence of temperature and size of the second phase particles.

Crack shielding

Crack-tip shielding effect applies to cases where a transformation of the second phase particles or microcracking in a limited zone of stress concentration near a crack tip takes place.

Microcrack toughening. This toughening mechanism requires stress-induced microcracking within a limited zone of stress concentration near the tip of a relatively large crack. Microcracks occur around a main crack by the result of

combination of localized residual tensions and the stress field associated with crack tips in a brittle material. The local residual stresses may arise from misfit between neighboring grains in a polycrystal with thermal expansion anisotropy or from the second phase inclusions that undergo transformation or have different thermal expansion or elastic properties. When a main crack propagates through the brittle material under an applied stress, it advances by interaction and coalescence of the microcracks arrested in grain boundaries or inclusion interfaces. The microcracking at the tip of the crack or in regions of high stress concentration also can have a shielding effect on the crack tip by redistributing and reducing the average near-tip stresses. Evans [Eva78] has shown that spontaneous microcracking does not occur at grain boundaries or inclusions below a critical size, but an applied stress could induce microcracking at a subcritical size. The stress-induced microcracks within a region of stress concentration near the tip of a large crack contribute to toughening of the brittle materials. The residual stresses are relieved by the microcracks as they provide a dilatation governed by the volume displaced by the microcracks, or as they reduce the elastic modulus within the process zone. The dilatational component contributes even more to toughening [Eva84]. This component is usually very sensitive to temperature because residual stress is reduced at increased temperatures. The modulus contribution, on the other

hand, is temperature invariant at a range of low temperatures. Computer simulation calculations of the interaction between a main crack and microcracks surrounding its tips have been done by Hoagland and Embury [Hoa80], using an image force to account for compliance effects. Microcrack parameters also have been extensively measured in ceramic materials (e.g., Al_2O_3 toughened with monoclinic ZrO_2) [Rue87].

Transformation toughening. The stress-induced transformation of particles in a limited zone of stress concentration near a crack tip reduces stress concentration near the crack tip. The transformations that can cause such toughening include martensitic transformation in ZrO_2 [Eva86a, Lan82], ferroelastic transformation [Vir86], and twinning. Two approaches have been used to analyze transformation toughening: a thermodynamic model [Bud83, Mar83] and a mechanics model [Eva80]. The analyses indicate that the steady-state toughness increase, ΔK_c, can be expressed by [Bud83, Eva80, Mar83]

$$\Delta K_c = \gamma E e^T V_f \sqrt{W} \qquad (2.17)$$

where γ is a constant, e^T is transformation strain, E is elastic modulus, V_f is volume fraction, and W is width of the transformation zone. The fracture toughness values of the transformation-toughened composites also depend on temperature [Bec87].

Crack bridging

Substantial toughening of brittle phases is possible by bridging of the main crack surfaces by unbroken ligaments of the reinforcements. The bridging imposes a closure force on the crack and restrains crack opening, or reduces crack-tip stresses, thereby yielding an increment in toughness over that of the matrix. The bridging ligament may be an elastic phase in the forms of whiskers, platelets, or fibers; a ductile metal [Xia91, Xia92a]; or coarse bridging grains in noncubic monolithic systems such as alumina [Pre86]. The increase in toughness of the composite can be obtained by [Eva86b, Bud88]

$$\Delta G \;=\; V_f \int_0^{u^*} \sigma(u) \, du \qquad (2.18)$$

where $\sigma(u)$ is the nominal stress carried by the bridging ligaments for a given crack opening, u is crack opening, and u^* is the crack opening at the point when the ligament material fails.

The crack surfaces are bridged by elastic stretch of the ligaments and interface frictional forces between the matrix and ligaments, when elastic ligaments bridge in the crack wake. The bond strength at the interface between the fiber and matrix imparts the toughening mechanism in a brittle matrix composite with brittle fibers. In the absence of interfacial

debonding, the crack-opening displacement will be limited by elastic displacement in the reinforcement across the crack surfaces when the crack front moves past the reinforcement. This displacement is extremely small and limited by the elongation of the reinforcement. If the reinforcement and matrix have comparable toughness, the composite is brittle and follows the rule of mixtures as discussed previously.

If interfacial debonding occurs, greater crack-opening displacements are achieved within the bridging zone, yielding larger toughening effects. Debonding reduces the amplitude of the stress concentration at the fiber along the matrix crack front and, when sufficiently extensive, allows the crack to circumvent the fiber, leaving the fiber intact in the crack wake and creating new surface at the interface zone.

Crack bridging by ductile ligaments. Significant increase in toughness of a composite is contributed by plastic stretching of ductile ligaments in the crack wake [Ell88, Mat89, Xia90]. The toughness increases with length of the ductile bridge zone and eventually realizes a steady-state level at a maximum bridge length governed by ligament rupture [Ash89]. At the steady state, the increase in toughness, ΔG_c, is given by

$$\Delta G_c = V_f \sigma_0 r \chi \qquad (2.19)$$

where σ_0 is the uniaxial yield stress of the ligament, V_f is

the volume fraction, and r is a radius of the ductile ligament. χ is a normalized work of rupture, which is given by

$$\chi = \int_0^{u^*} \frac{\sigma(u)}{\sigma_0} \cdot \frac{du}{r} \qquad (2.20)$$

χ depends on the constraint and thus on the strength of the fiber-matrix interface. From the above relationship, the increase in toughness is expressed by

$$\Delta K = [\chi V_f E \sigma_0 a_0]^{1/2} \qquad (2.21)$$

Therefore, the amount of toughening enhancement depends on the volume fraction of ductile ligaments, length of bridging zone, and size of ligament. Toughening increase is obtained by fiber rupture due to expenditure of energy in plastic deformation. Sometimes plastic deformation may not be fully utilized due to fiber embrittlement which may occur during fabrication or service. Higher work-hardening capacity of the fiber can contribute to increase in toughness.

Although several toughening micromechanisms have been discussed as listed previously, fracture of a material generally cannot be motivated by a single fracture mechanism, but multiple micromechanisms are responsible for the material failure. Crack shielding in the process zone related to

stress-induced transformation or generation of microcracking will be difficult to contribute to toughening in intermetallics like the titanium aluminide group. In contrast, crack bridging by ductile ligaments is expected to play a major role in toughening the brittle intermetallics. However, the sacrifice of stiffness and strength of the composite should be considered when a ductile phase is loaded.

Effect of Thermal Residual Stress

Alumina fiber, niobium, and the matrix alloy used in the composites have different coefficients of thermal expansion. As such, temperature changes during processing and/or service use would induce thermal residual stresses in the composites. When the constituting phases of a composite are heated to the processing temperature, each component expands by $\alpha_i \cdot \Delta T$ under no constraint, with α_i being thermal expansion coefficient of the individual component i and ΔT being the temperature change. After processing of the composite, however, thermally induced residual internal stresses develop as a result of the strain constraint imposed by the constituting phases on each other. The matrix has a higher coefficient of thermal expansion than the reinforcement, and $\Delta\alpha$ is negative; thus, a large thermal strain can be developed in a temperature interval during cooling. As such, upon cooling, the fiber will be compressed in the radial direction and the matrix will be in tension.

The thermal strain, ε_T developed in the composite upon cooling to the temperature, T is expressed as

$$\varepsilon_T = \int_{T_0}^{T} \Delta\alpha \, dT \qquad (2.22)$$

where $\Delta\alpha = \alpha_f - \alpha_m$, α_f and α_m being the linear thermal expansion of fiber and matrix, respectively. T_0 is stress-free temperature and T is the testing temperature. The residual stress at the interface between the fiber and matrix due to the thermal expansion mismatch can be estimated assuming that the components remain elastic [Jan91, Bud86]. The axial residual stress in the fiber is expressed as

$$\sigma_z^T = -\frac{\lambda_2}{\lambda_1} \frac{E_f E_m}{E_c (1-\nu_m)} (1-V_f) \varepsilon_T \qquad (2.23)$$

where ν_m is the matrix Poisson's ratio, ε_T is thermal strain, and λ's are coefficients that depend on the elastic constants. If $\nu_m = \nu_f = \nu$,

$$\lambda_1 = 1 - \frac{1-2\nu}{2(1-\nu)} (1-\frac{E_c}{E_f}) \qquad (2.24)$$

and

$$\lambda_2 = \frac{1}{2} (1+\frac{E_c}{E_f}) \qquad (2.25)$$

The residual stress on the outside surface of the fiber in radial direction, $\sigma_r{}^\mathsf{T}$, and in circumferential stress $\sigma_\theta{}^\mathsf{T}$ is

$$\sigma_r^T = \sigma_\theta^T = -\frac{E_m}{2\lambda_1(1-\nu_m)}(1-V_f)\,\varepsilon_T \qquad (2.26)$$

The above formulas show how much thermal residual stress develops in a composite due to CTE mismatch between reinforcement and matrix. The effect of such residual stress on measured mechanical properties will be discussed later.

CHAPTER THREE
EXPERIMENTAL PROCEDURES

Procedures for the preparaing composite samples and observing their chemical stability and mechanical properties are described in this chapter.

The composites were fabricated from mixtures of Al-25Ti-25Ta matrix and reinforcements of short niobium fibers and/or alumina fibers by vacuum hot pressing at 1573 K. To prevent interaction between the matrix and niobium, alumina coating on the fibers was provided by either a sol-gel dipping process or an in-situ oxide formation technique. The mechanical properties of the composites were measured by four-point bend testing at room temperature and high temperatures. The following describe the experimental approach used to synthesize and characterize the mechanical behavior of the composites.

Starting Materials

Matrix Material

The matrix material used for fabrication of composites was Al-Ti-Ta alloy powder developed and supplied by Pratt & Whitney, West Palm Beach, Florida. The alloy was arc-cast and converted to powder using VORTEC milling at 20,000 rpm. The

nominal composition of the powder was Al-25%Ti-25%Ta, which consisted of two phases, σ and γ.

The as-received powder was analyzed for size distribution, shape, density, and specific surface area before further processing. An example of the alloy powder, observed under a scanning electron microscope[1], is shown in Figure 3.1. In general, the shape of particles was irregular and their surfaces were rough, with some containing cracks. The powder size distribution was analyzed by a sedimentation method using an X-ray sedigraph[2], and the result of the analysis is summarized in Figure 3.2. The median diameter of the powder was 15.7 μm. The surface area of the powder was 0.291 m^2/g when analyzed by the Brunauer-Emmet-Teller (BET) method using nitrogen gas. The density of the powder measured by a pycnometer was 6.96 x 10^6 g/m^3.

Reinforcement Materials

For the chemical stability study, various types of ceramic materials were initially reviewed and screened as candidates for reinforcement or coating materials. To investigate the chemical interaction between candidate reinforcement and matrix material, composites were made by vacuum hot pressing mixtures of the matrix powder and

---

[1] JEOL JSM-35CF, JEOL Ltd., Tokyo, Japan.

[2] Particle Size Analysis System, Model Sedigraph 5100, Micromeritics Instrument Corp., Norcross, Georgia.
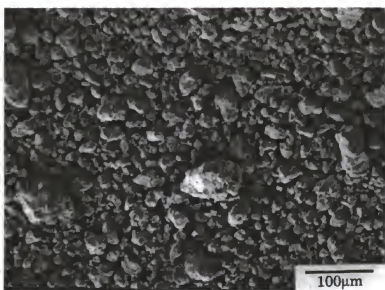
Figure 3.1 Magnified view of Al-Ti-Ta alloy powder.
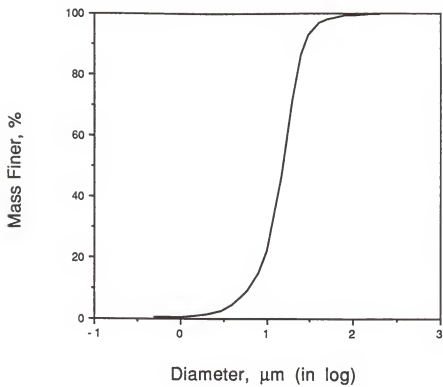
Figure 3.2 Particle size distribution of matrix alloy powder.

candidate materials in whatever shape they were commercially available. Sources and properties of the analyzed candidate materials are listed in Table 3.1.

Alumina fiber

Fiber FP is a commercial alumina fiber that has been used to fabricate metal matrix composites. The FP fiber is not only compatible with many metals but also exhibits a high modulus and strength, which are retained to high temperatures [Pys89, Dhi80].

The as-received continuous FP yarn was cut into approximately 100-mm-long fiber bundles. Their organic sizing was burnt by heating in a quartz tube, which was placed in a Lindberg tube furnace at 948 K for 1 h. The surface of the baked fibers was examined using scanning auger spectroscopy[3], but no element except Al and O was detected. The fiber bundles were then chopped into short fibers with an average aspect ratio of 15. The micrograph of the chopped alumina fibers is shown in Figure 3.3. The chopped fibers were classified to remove fine particulate matter as well as undersized and oversized fibers. This was achieved by sieving the chopped fibers through stacked wire cloth sieves[4] of three standard sizes (60, 80 and 270 mesh). While sieving may not be a perfect method to eliminate improper size fibers, it was found

---

[3] Perkin-Elmer PHI 660 Scanning Auger Multiprobe, Physical Electron Div., Perkin-Elmer Corp., Eden Prairie, Minnesota.

[4] Newark Wire Cloth Co., Newark, New Jersey.

Table 3.1 Reinforcement materials
         investigated for chemical stability

Reinforcement phase	Material form	Composition	Material source
Al_2O_3	fiber (Fiber FP)	99.0%	Du Pont[a]
Y_2O_3	powder	99.0%	Cerac[b]
ZrO_2	fiber (Z3Y13)	ZrO_2 - 3 mol% Y_2O_3	University of Florida
	fiber (ZYF50)	99.0% ZrO_2	Zircar Products[c]
ZrN	powder	99.5%	Cerac
TiN	powder	99.5%	Cerac
ZrC	powder	99.5%	Cerac
TiC	powder	99.5%	Cerac
SiC	platelets, -16,+20 mesh	99.9%	American Matrix Inc.[d]
TiB_2	powder	99.0%	Cerac
BN	powder	99.5%	Cerac
Nb	wire	99.8%	California Fine Wire[e]

a: E.I. du Pont de Nemours and Company, Inc.,
   Wilmington, Delaware
b: Cerac Inc., Milwaukee, Wisconsin
c: Zircar Products Inc., Florida, New York
d: American Matrix Inc., Knoxville, Tennessee
e: California Fine Wire Co.,
   Grover City, California

helpful in significantly reducing the agglomeration of fibers during subsequent mixing and dispersion processes. A few long fibers passed through the sieves in their axial directions, but they were eliminated by repeating sieving several times so that a small fraction of fibers in the range of +270 -80 mesh was separated. Repeating the sieving process three times yielded approximately 41% of the starting material. The fractionated fibers were stored for later use.

To calculate a range of aspect ratios of fibers, the length distribution of a sample of the chopped fibers was analyzed by dispersion of the fibers in water followed by drying on slide glasses. The dried fibers were photographed in a light optical microscope[5], and then the lengths of the fiber images shown on enlarged photograph print papers were measured. The length distribution of the fibers is shown in Figure 3.4. The size analysis resulted in a median length of 245 μm, and the average aspect ratio was calculated as 13.3.

Other ceramic ingredients

The other ceramic materials used in the investigation of chemical compatibility were commercial powders of yttria, zirconium nitride, titanium nitride, zirconium carbide, titanium carbide, silicon carbide, boron nitride, and titanium boride. A sample of yttria(3 mol.%)-doped zirconia fibers made at the University of Florida [Sim90] also was used. The

---

[5] Nikon Model EPIPHOT-TME, Nippon Kogaku K.K., Tokyo, Japan.
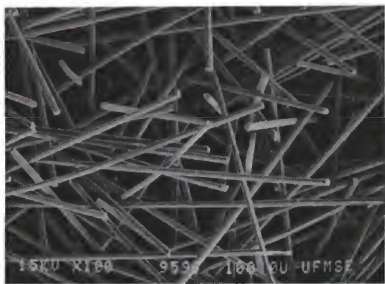
Figure 3.3 Chopped FP alumina fibers from E.I. du Pont de
Nemours and Company, Inc..
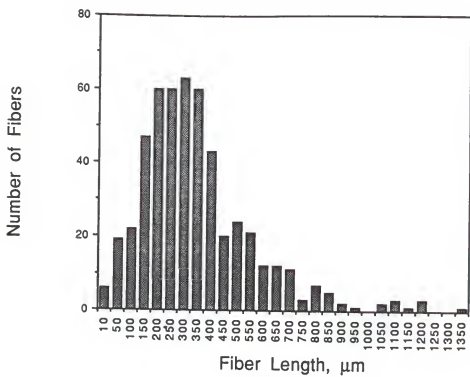
Figure 3.4 Length distribution of chopped alumina fibers.

sources and characteristics of the reinforcement materials used in this investigation are listed in Table 3.1.

Niobium fibers

The niobium fiber with a diameter of approximately 0.125 mm was supplied by California Fine Wire Co., Grover City, California. The fiber was cleaned in three steps to remove oil, grease, or other surface contaminants. The fiber was first dipped in chloroform in an ultrasonic cleaner for 5 min, and then dipped in a KOH solution at a concentration of 60 g per 100 ml of water kept at 343 K. After soaking in the solution for about 3 min, the fiber was immediately rinsed with a jet of tap water to blast off any loosened scale and attached salts. After alkaline cleaning and rinsing, the niobium fiber was cleaned further with an acidic solution at room temperature. The solution consisted of 50 vol.% of a concentrated nitric acid, 15 vol.% of a concentrated hydrofluoric acid, and the remainder water. After acid pickling, the fiber was washed thoroughly with water and dried in air.

The cleaned niobium fiber was cut to about 3-mm-long pieces. Using scissors caused slight bending at the ends of the pieces, making them unsuitable for the subsequent extrusion process. As the bent fiber agglomerated and impeded the narrow slit of the extruder and prevented further processing. In order to avoid this, a bundle of fibers was cast along the axial direction in a glass tube and epoxy

resin. The cast polymer composite containing the niobium fibers was ejected from the tube and sliced into disks containing approximately 3-mm-long niobium fibers with a diamond blade using a water-based coolant. The polymer matrix was dissolved in a solvent and the niobium fibers were extracted by filtration.

Coating on Niobium Fibers

Niobium was found to react with the matrix alloy at high temperatures. To prevent interaction between niobium and the matrix, the metal fibers were coated with a protective layer of alumina. The coating was produced by either sol-gel processing or by an in-situ oxide formation technique during consolidation of the composites.

For the former process, the niobium fibers were coated by dipping them into an aluminum alkoxide sol prepared by the procedure described in Clark et al. [Cla88]. The fibers were dried to gelate the sol coating of aluminum monohydrate, $AlO(OH)$ on the metal fiber. A solid coating was obtained after pyrolysis of the dried coating in air at 623 K for 0.5 h. The coated niobium wires were cut and mixed with the matrix alloy powder. The mixture was hot pressed and then annealed by the procedures applied in the investigation of thermochemical stabilities of the other materials, as described in the section on "Hot Pressing".

For the latter process, alumina coating on short niobium fibers was synthesized in situ during compositing. The process is described in detail in the work by Lu et al. [Lu90a, Lu90b]. The chopped fibers were put into a quartz tube and heated at 723 K in a tube furnace under flowing oxygen gas atmosphere at a flow rate of 15 cc/min. The fibers were heated for 15 min, while the quartz tube was rotated at 60 rpm by a DC motor to dissipate the reaction heat and produce uniformly oxidized niobium fibers. Depending on the heating time, color of the oxidized surfaces became dark blue and then dark gray. The coating finally changed to white as the oxidation layer became thick. The pre-oxidized metal fibers were mixed with the matrix alloy and hot pressed. As described by Abbaschian and his co-workers [Lu91, Dot93, Dot94], the oxide scale on the niobium fibers was converted to alumina during hot pressing.

Alignment of Reinforcements

The alignment of discontinuous alumina fibers and niobium fibers in composites was achieved by extrusion of the dispersion of the reinforcements and matrix powder in a highly viscous polymer solution.

The solution was prepared by dissolving ammonium alginate powder in water in the weight ratio of 2:100. This process was conducted by adding alginate powder to water while stirring the solution to avoid formation of a lumpy solution. The

matrix powder and the chopped alumina fibers and/or niobium
fibers were dispersed in the alginate sol by adding a small
amount at a time into the continuously stirred solution.
Vigorous stirring was avoided to minimize entrapped air
bubbles in the suspension during mixing. After loading of the
desired amount of alumina and/or niobium fibers, the matrix
powder was added to the suspension and mixed in the same way.
The volumetric ratio of solid components to the alginate
solution in the final suspension was 5:100. The suspension was
finally extruded immediately through a 22.3mm x 0.95mm nozzle
(the area reduction ratio is about 1:10) at a constant flow
rate.

The extruded tape was dipped in 1 % HCl solution, causing
the alginate tape to gelate and to have adequate strength for
further handling. The gel tape was washed in flowing water,
dried in air at room temperature for 24 h, and cut into
rectangular sheets with a dimension of approximately 35mm x
30mm. The sheets were stacked with the fibers aligned in one
direction. The stack was cut into a cylindrical shape to fit
in the hot press die. Once loaded, the die was placed in an
oven at 473 K for 1 h to remove the polymer and any remaining
moisture from the stack before hot pressing.

Hot Pressing

Consolidation of the matrix alloy powder or composites
was done by vacuum hot pressing mixtures of the matrix powder

and short fibrous reinforcements in an induction heating furnace.[6] The die assembly used for hot pressing, shown in Figure 3.5, which was machined from isostatically pressed graphite rods.[7] The dimensions of the die body were I.D. 38.2 x O.D. 76.2 x height 76.0 mm. The die was wrapped with three layers of graphite felt and placed in a translucent quartz cylinder with dimensions of I.D. 139 x O.D. 158 x height 178 mm. Boron nitride powder[8] suspended in ethanol by ball milling was applied on the graphite sheets inserted in the die cavity. A binder-removed insulation oxide sheet[9] was used as a thermal insulation between the charge and pistons, between the pistons and ram, and between the die and support block.

Mixtures of the powder and fibers were hot pressed under vacuum of 1.3×10^{-2} Pa into disk shapes. Pressure generated from a hydraulic system was applied to the charge from the top direction. The temperature during hot pressing was measured using thermocouples and a calibrated infra-red two-color optical pyrometer[10] focused on the graphite die.

---

[6] Centorr Hot Press Furnace Model 600-6x5IND6-25, Centorr Associates, Inc., Suncook, New Hampshir.

[7] Poco Grade HPD-1, Poco Graphite Inc., Decatur, Texas.

[8] ZYP Coatings, Inc., Oak Ridge, Tennessee.

[9] Fiberfrax 970 sheet, The Carborundum Company, Niagara Falls, New York.

[10] Model: Ratio-Scope ROS-8DD, CAPINTEC Instruments Inc., Ramsey, New Jersey.

Optimization of Hot Pressing Condition

The optimum hot pressing condition to yield dense samples from the alloy powder was determined after a series of vacuum hot pressing runs were conducted under a set of different parameters such as temperature, pressure, and time. The consolidation times selected were 1/4, 1/2, or 1 h at temperatures of 1473, 1573, and 1673 K. The applied pressure of 3.45×10^7 Pa was selected because of the strength of the graphite die. The microstructure of the hot-pressed samples was investigated, and their densities were determined either by the Archimedes method [AST93c] using deionized water. Figure 3.6 shows the result of the investigation on densification as function of pressing time at two temperatures. The samples processed at 1473 K were not densified fully and contained large volumes of pores. However, samples hot pressed at 1573 and 1673 K were close to full densification with a little amount of small voids around previous particulate boundaries. Therefore, the optimum condition of hot pressing of the composites was selected as pressing time of 1/2 h under 34.5 MPa pressure at 1573 K. Following the hot pressing, the specimens were furnace cooled. Thermomechanical history during hot pressing is shown in Figure 3.7.

For fabrication of samples for investigating chemical reactions, typically 15 vol% of the reinforcement was mixed
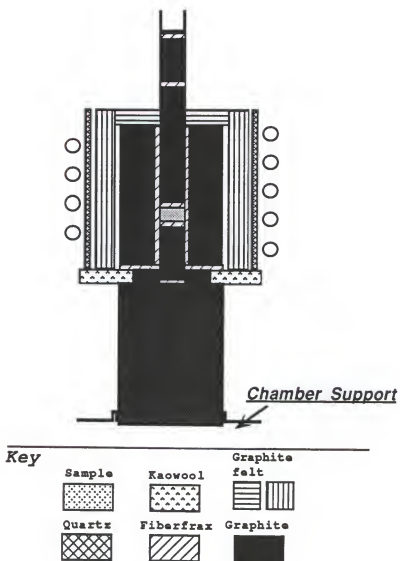
Figure 3.5 Schematic of hot-press die arrangement.
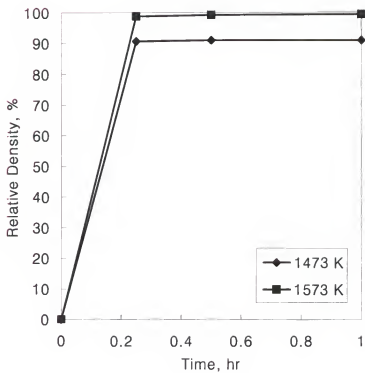
Figure 3.6 Densification in variation with hot-pressing time
at various temperatures under 34.5 MPa pressure.
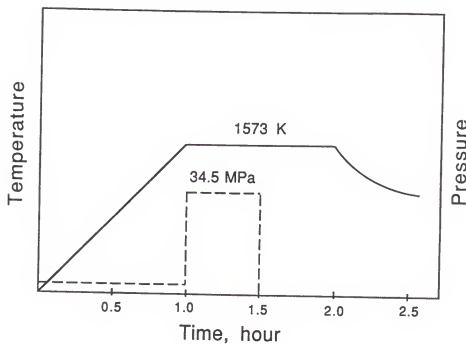
Figure 3.7 Thermomechanical history diagram during typical hot pressing of composites.

with the matrix powder and the mixture was hot pressed into disk-shaped samples. Pieces were cut from the disks with typical dimensions of 38.2 mm diameter x 4.0 mm height. They were covered with a thin tantalum foil and annealed in a tube furnace for 50 h at 1573 K while Ti-gettered Ar was flowing.

To fabricate composite specimens for the measurement of their mechanical properties, mixtures of the matrix powder and short fibers were hot pressed under the same condition as above. Stacks of extruded sheets containing the alloy powder and aligned short alumina and/or alumina-coated niobium fibers were charged into the graphite die and hot pressed. Typical dimensions of the hot-pressed specimens were 38.2 mm diameter x 7.6 mm height.

Microstructure Characterization

The hot-pressed or post-annealed samples were cut by a diamond saw, mounted in an epoxy, and polished using standard procedures. A modified Kroll's etchant (10ml HF, 14ml HNO_3, and 76ml water) was used for etching the specimens. The microstructure of the alloy and composites was analyzed by light optical microscopy and scanning electron microscopy. Volume fraction of the matrix phases was analyzed by a digital image analyzer.[11]

Composition change across the interfaces between the matrix and reinforcement materials was analyzed by electron

---

[11] Model QUANTIMET 520, Cambridge Instruments

probe microanalysis (EPMA).[12,13] Quantitative concentration analysis of elements was done by energy dispersive spectroscopy (EDS) and light elements were analyzed by wavelength dispersive spectroscopy (WDS) with the activation energy of 20 KeV. A PRZ correction program was used to treat raw composition data. Concentration of light elements, such as C, N, and O, was calculated from the balance of metal elements. For calibration of the microprobe, pure metals (99.9 % purity) and monolithic ceramic phases (99.9% purity) were used as the standards.

Mechanical Testing

Flexural properties of the specimens were measured at room and elevated temperatures. Chevron-notched bend samples were tested at room temperature to compare fracture toughness values of the composites.

The test procedures were adapted from available industrial standards for ceramics. The procedures are the most useful for studying brittle and composite materials when it is difficult to conduct direct tensile testing. Since flexural testing of composites has not been thoroughly standardized, the standards for brittle ceramics [JSA81, USD83] or rigid plastics [AST93a] have been frequently used for characterization. ASTM recently established standard test

---

[12] Tracor Northern TN-5500 X-ray Analyzer microprobe

[13] JEOL Superprobe 733, JEOL Ltd., Tokyo, Japan.

methods for flexural strength of advanced ceramics at ambient [AST93d] and elevated temperatures [AST93e]. The transverse loads in flexural tests of materials are usually applied by one (three-point loading) or more (e.g., four-point loading) concentration forces. The four-point loading configuration is considered more reliable than the three-point loading for determination of the elastic modulus [Ham71] because of uniform state of stress over the entire gauge length, absence of contact stresses at the point of application of concentrated forces (i.e., at load and support points), and elimination of overhanging effect. In this study, four-point flexural testing was conducted on three specimens with a rectangular cross section for each given condition unless noted otherwise.

Preparation of Test Specimens

Flexural test specimens with approximate dimensions of w 4.0 x b 1.2 x L 25 mm were prepared from hot-pressed disks. The specimen thickness was selected so as to include several layers of reinforcements (alumina fibers of 0.018 mm diameter or niobium fibers of 0.125 mm diameter). The specimens were cut by a diamond saw from the hot-pressed disks, as shown in Figure 3.8, such that the longitudinal axis of the cut specimen bar would be parallel to the reinforcement alignment direction. The specimen surfaces were ground, and the tensile surface of the bar was polished using 1 μm alumina powder. The

four long edges of each specimen were rounded by grinding on
a 400-grit SiC grinding paper.

Toughness test specimens were prepared from the hot-
pressed disks as depicted by figures 3.8 and 3.9. Chevron-
notched bar specimens with approximate dimensions of w 4.0 x
b 2.5 x L 25.0 mm were cut from the hot pressed disks in the
same way as the flexural test bars. Then, a chevron-shaped
notch with width of about 0.2 mm was introduced at the center
of the bars using a 0.15-mm thickness low-speed diamond saw
(see Figure 3.9).

Room Temperature Testing

At room temperature, a screw-driven universal tester[14]
was used to perform four-point flexural tests at a cross-head
movement rate of 0.002 in/min (or 0.000847 mm/s). A bend test
fixture[15] with an outer span of 20.00 ± 0.10 mm and inner
span of 10.00 ± 0.10 mm was used. The loading scheme of test
specimen bars in four-point flexural test is shown in Figure
3.10. A reversible tension-compression load cell with an
operative range of 5000 lbf (2.22 x 10^4 N) was used at a 200-
lbf (8.90 x 10^2 N) scale with an accuracy of ± 0.04%. A
calibrated Instron extensometer was used to monitor
displacement during testing. Voltage signals representing load

---

[14] Instron model no. 1125, Instron Corporation,
Canton, Massachusetts.

[15] Model 642.05A-01 and 642.05A-02,
MTS System Corporation, Minneapolis, Minnesota.
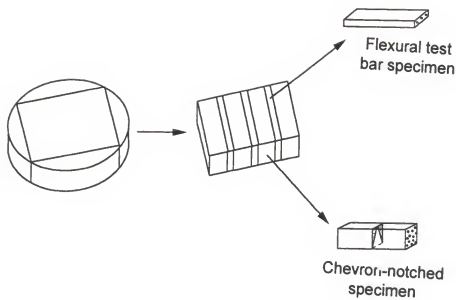
Figure 3.8 Preparation of flexural test bar and chevron-notched test specimens from a hot-pressed disk sample.
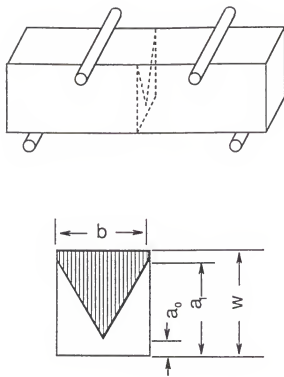
Figure 3.9 Schematic of a four-point flexural test specimen with a chevron-shaped notch used for fracture toughness test. Its average dimensions are $a_0 = 1.2$, $a_1 = 3.7$, $b = 2.5$, and $w = 4.0$ mm.
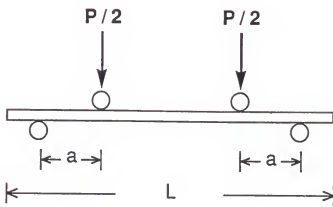
Figure 3.10 Loading scheme of a specimen bar for four-point flexural test. a = 5 and L = 25 mm. Average dimensions of the test specimen are w = 4.0, b = 1.2, and L = 25 mm.

and displacement change were acquired using a data acquisition system with a 12-bit A/D converter and an IBM personal computer.

Elevated Temperature Testing

The flexural test at elevated temperatures was done on a servo-hydraulic-driven universal tester[16] with an atmosphere-controlled furnace. A low-capacity, 200-lbf (8.90 x 10^2 N) load cell was used with 100-lbf (4.45 x 10^2 N) test range with an accuracy of $\pm$ 0.010% of the full-scale range to measure applied loads. The fixture for the high-temperature flexural testing was made of SiC, as shown in Figure 3.11. The lower pins sitting in V grooves were 20.0 mm apart, which resulted in a span-to-thickness ratio of about 17. A 0.125-mm-thick graphite sheet[17] was inserted between the specimen and the fixture pins to decrease friction at the support and to prevent direct contact and reaction at high temperatures. Before testing specimens, the compliance of the system at each test temperature was measured by compression tests without placing a specimen.

The ductile-to-brittle transition temperature of the matrix alloy was found between 1073 and 1273 K, after testing preliminarily the material at several temperatures in the

---

[16] MTS Material Test System model 810, Minneapolis, Minnesota

[17] Grafoil Grade GTA, Union Carbide Corp., Cleveland, Ohio.
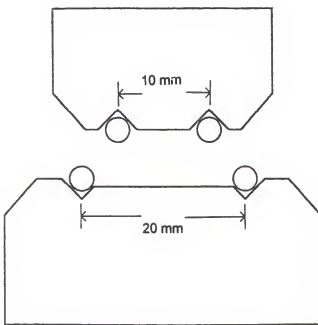
Figure 3.11 Four-point flexural test fixture made of silicon carbide
and used for high temperature test.

range of 1073 to 1573 K. The flexural testing was conducted at 1273 and 1473 K, at which temperature the matrix was considered to yield before failure. Before testing, the specimens were heated under vacuum of 1.33 x 10^{-2} Pa in the furnace[18] mounted on the MTS loading frame. The furnace temperature was measured by B-type thermocouples placed in the vicinity of the specimen. The furnace was heated at a rate of 50 K/min (0.83 K/s) up to the test temperature. Testing started 20 min after the temperature reached the desired level to allow for thermal stabilization in the furnace.

A small load of about 4.4 N was applied to hold the specimen during heating to allow for thermal expansion of the sample and fixtures. The force control mode was switched to the displacement control mode just before running the test. The displacement control rate was maintained as 2.54 X 10^{-2} mm/s during the test. The crosshead was stopped before displacement of 4 mm, which was the deflection limit of the fixture.

Load and displacement data were acquired in the same manner as in the room temperature test. A microcomputer, interfaced with the MTS test frame control console, was provided for digital data acquisition. At periodic intervals (data acquisition rate of 4 Hz) traces of load versus displacement were recorded.

---

[18] Model FR200, Oxy-Gen Industries Inc., Epsom, New Hampshire.

Processing of Flexural Test Data

In a typical load-deflection curve, there was an artifact called a toe region due to a takeup of slack, and alignment or seating of the specimen during loading. This artifact was compensated for according to ASTM D790 [AST93b] to determine the corrected zero point on the displacement axis.

In processing the results of the four-point flexural tests, the deflection of a prismatic bar, δ, at midspan was estimated by using the following equation [Tim70]

$$\delta = \frac{Pa}{4bh^3E}(3L^2-4a^2) \qquad (3.1)$$

where E is modulus of elasticity, P is applied load, a is distance from the support roller to the load applicator, b is specimen width, h is specimen thickness, and L is outer span length. Thus, the modulus of elasticity in bending under four-point loading, E_b, can be calculated with the known load increment, ΔP, and the corresponding deflection increment, $\Delta\delta$, between two points in the Hookean region of the load-displacement curve, using the formula:

$$E_b = \frac{a(3L^2-4a^2)}{4bh^3}\frac{\Delta P}{\Delta\delta} \qquad (3.2)$$

The maximum stress, σ, in the outer fibers of a specimen in its gage length for an applied load and relatively small

deflections is determined by the formula [Tim70, Tar81]:

$$\sigma = \frac{M}{W} \tag{3.3}$$

where M (= P·a/2) is the bending moment, and W (= $bh^2/6$) is the resistance of cross section of the specimen. Thus, the maximum stress is calculated by

$$\sigma = \frac{3Pa}{bh^2} \tag{3.4}$$

When a specimen fails in a brittle manner during testing, the flexural strength is equal to the maximum stress in the outer fibers. Therefore, the flexural strength or modulus of rupture of the specimen, σ_b, was calculated in accordance with eq. (3.4) by setting P equal to the applied peak load. However, if the specimens is not brittle and yields before failure, the value of P should be determined by the following method.

When the specimen deformed extensively prior to failure at high temperatures, flexural strength comparison was made by the estimation of the flexural stress at a strain level of 0.01% in the outer span of the specimen [AST93b]. Thus, the flexural offset yield strength was calculated in accordance with eq. (3.4) by setting P equal to the load at the permanent deflection. The value of the permanent deflection, δ_p corresponds to the permanent strain in the outer surface of 0.01% and was calculated at the load applicator [Tar81] by

$$\delta_p = \frac{0.0001(3La-4a^2)}{3h} \qquad (3.5)$$

The deflection at midspan could not be measured directly because of the closed atmosphere-controlled furnace. Therefore, the displacement at the load applicator position on the specimen was assumed the same as the crosshead movement of the test machine.

When support span-to-depth ratio, L/h was greater than 16 to 1 and resultant deflections occurred in excess of 10 % of the support span, the peak stress was approximated based on the change in the outer span L and the distance **a** as [AST93b]

$$\sigma = \frac{3Pa}{bh^2}(1-10.91\frac{\delta h}{L^2}) \qquad (3.6)$$

In this caes, the modulus of elasticity in bending, E_b, was estimated with the known load increment, ΔP, and the corresponding deflection increment, $\Delta \delta$, measured at the load applicator positions as

$$E_b = \frac{a(3La-4a^2)}{bh^3}\frac{\Delta P}{\Delta \delta} \qquad (3.7)$$

The load cell of the MTS system was so sensitive that it picked up noise signals from various sources, such as vibration of the system, unsteady pressure, and flow rate of

the furnace coolant or the driving hydraulic system during testing. Moreover, the predominant error source was the induction current field generated by a.c. electrical heating elements and furnace power lines. The actual load-deflection curve was determined from the noisy data -- some with significantly high amplitudes. In addition, there was a group of signals with a certain range of frequencies and amplitudes that appeared in the load-deflection curves of most of the specimens tested at the high temperatures. The noise patterns on these load-deflection curves were subtracted from the acquired data values. The load-deflection curve after removing the noise signals was smoothed further by a regression method using a computer program. Then, the actual load-deflection curve was obtained by compensating for the deflection of the system including deformation of the fixture. The deflections of the system measured at 1273 and 1473 K are shown in Figures 3.12 and 3.13 and the regressions of the curves were

$$P_{S,1273} = 0.3425 + 119.3\delta - 678.1\delta^2 + 22880\delta^3 \quad (3.8)$$

and

$$P_{S,1473} = 0.6904 + 45.63\delta - 3995\delta^2 + 21980\delta^3 \quad (3.9)$$

respectively, where P is the load in kgf and δ is displacement in mm. To provide improved resolution for determination of nonlinear displacement-load behavior, load versus differential
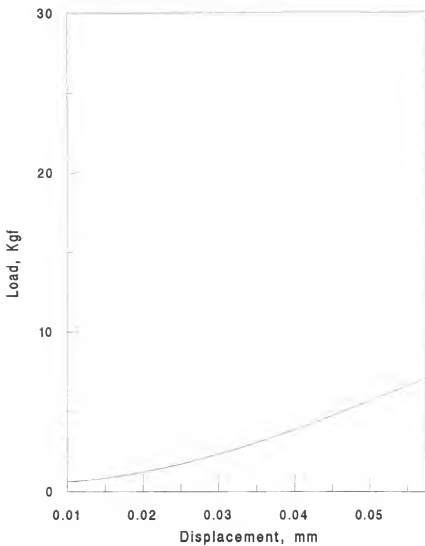
Figure 3.12 Load-deflection curve of the testing system at the test temperature, 1273 K.
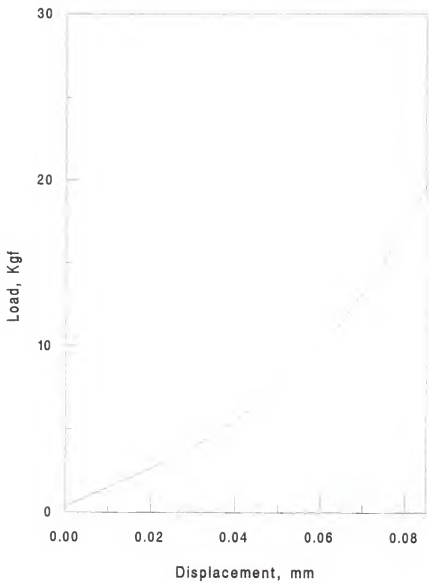
Figure 3.13 Load-deflection curve of the testing system at the test temperature, 1473 K.

displacement traces also were produced. Differential displacement is the difference between the actual displacement value and the one from the linear fit at the same load level. The differential displacement value is then multiplied by a factor of 5 to show any nonlinear behavior in detail.

Fracture Resistance Calculation

The toughness of the AlTiTa alloy matrix and the composites wre measured by four-point bending test of chevron-notched specimens, with an inner and outer span of 10 and 20 mm, respectively. The peak load of bending was used to calculate fracture toughness of the specimens using the following formula

$$K_{IC} = \frac{P_{max}}{bw^{1/2}} Y^*$$ (3.10)

where P_{max} is the maximum applied load, and b and w are thickness and width of the specimen, respectively. Y^*_{min} is the minimum value of the stress intensity factor coefficient, which is a function of a crack length for the particular specimen used [Mun80]. Because of rising crack-growth resistance for ductile-phase-toughened composites [Xia92c], P_{max} and Y^*_{min} do not occur coincidentally at the same crack length. Therefore, P_{max} does not precisely correspond to the stress intensity factor at failure but a good

approximation to it [Mun81, New84, Sha84]. As such, the value estimated using eq. (3.10) is called damage tolerance in this work and designated as K_{max}. These values were compared with the concept of work of fracture.

Fracture resistance of the composites was quantified using the work of fracture. This measurement involved calculating the area under the load-displacement curves from flexural tests of chevron notched specimens, and dividing by twice the fracture area of the specimen, such that [Jen92, Tat66]

$$\gamma_{WOF} = \frac{1}{2A} \int P d\delta \qquad (3.11)$$

where γ_{WOF} is the work of fracture, P is the applied load, δ is displacement, and A is the fractured surface area of the specimen.

Fractography

Following mechanical testing, the fracture surfaces were cleaned in an ultrasonic bath using a sequential process of ethyl alcohol and acetone baths. The samples were then mounted on SEM stubs and coated with Au-Pd alloy. The treated fracture surfaces were examined using a scanning electron microscope.

CHAPTER FOUR
RESULTS

Microstructure of Matrix Material

The microstructure of the Al-Ti-Ta matrix alloy hot-pressed for 0.5 h at 1573 K is shown in Figure 4.1. The micrograph reveals that the material consisted of two phases: one with a low z number (dark) and the other a high z number (light). The composition of each phase was measured by electron microprobe analysis (EPMA) as Al-13.6% Ti-43.7% Ta for the light phase, and Al-29.7% Ti-15.3% Ta for the dark phase. The composition of the light phase falls in the sigma(σ) phase region and the dark phase in the gamma(γ) phase region of the ternary phase diagram depicted in Figure 4.2. The presence of these phases was confirmed by XRD peaks, which corresponded to TiAl (γ) and Ta_2Al (σ) structures. The volume fractions of the gamma and sigma phases were measured by the image analyzer as 67.2 vol.% and 32.8 vol.%, respectively. The bulk composition of the specimen was measured as Al-25.4%Ti-24.3%Ta in EPMA with an electron beam of approximately $50\mu m$ diameter. The microstructure of hot-pressed alloy was so sound that no precipitate like alumina was found.
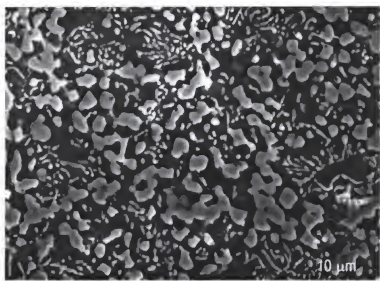
Figure 4.1 Microstructure of the hot-pressed matrix alloy.
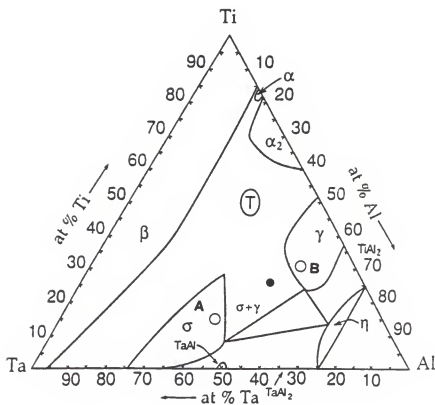
Figure 4.2   Isothermal section at 1473 K of Al-Ti-Ta ternary system [Dev91]. The matrix alloy consists of two phases, marked as 'A' and 'B', respectively. Its overall composition is represented as a ● mark.

Thermochemical Interface Interaction

The chemical reactions at the interfacial regions between reinforcements and the matrix in hot-pressed composites, which were annealed under an inert atmosphere for 50 h at 1573 K, were investigated. The results were used to select reinforcements that were compatible with the matrix.

Composites Reinforced with Oxides

The microstructure of the composites containing FP alumina fibers and yttria powder were free of a reaction product phase at the interface between the matrix and the reinforcements. Figure 4.3(a) shows an example of such an interface between alumina and the matrix, together with the EPMA composition profiles in Figure 4.3(b). The latter shows the Al, Ti, and Ta line scans across the interface. The concentration of oxygen could not be measured by EDS, but its existence in the core of the alumina fibers or yttria particles was confirmed by separate investigations using WDS. Thus, the concentration of oxygen was estimated as the balance of the EDS measurements. The compositional analyses are believed to be fairly accurate since the concentration of Al in the alumina fibers was measured as about 40 at.%, analogous to that measured by the same analytical method in a standard alumina sample. Also, the concentration of Y in the yttria particles was consistent with that of a standard yttria sample. Inside both reinforcements the concentrations of Ti

and Ta were below the measurement limit. Within the matrix, however, their concentrations changed between two levels corresponding to γ and σ phases. There was no evidence of a third phase in the interfacial regions. Furthermore, the composition change of these elements across the interfaces, if any, was limited within the spatial resolution of this analysis, about 2 μm, as electron beam size of about 1 μm was used. The microstructure and composition information showed that there was no reaction product between the FP alumina fiber and matrix or between the yttria particle and matrix when the samples were hot pressed and annealed for 50 h at 1573 K. The microstructure study and composition analysis did not show alumina or any other precipitates in the matrix.

In contrast to the above, examination of the composites reinforced with the yttria-stabilized zirconia fibers showed extensive interactions. Figure 4.4 shows a micrograph of the fiber embedded in the matrix and compositional scan line along the light bar in the photograph. The major constituents in the core of the fiber were Zr and O, with a small amount of Y. However, the irregular outer boundary of the fiber indicates that it has been eroded during processing and/or annealing. In addition, a continuous dark band was seen around the fiber which had the molar ratio of Al to O of approximately 2 to 3 and contained a small amount of Zr. This molar ratio is close to that of the standard alumina sample. In the area between the eroded fiber and the dark band, the concentration of Al
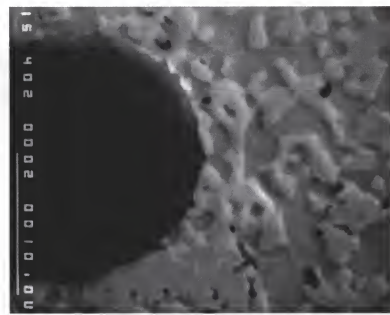
(a)
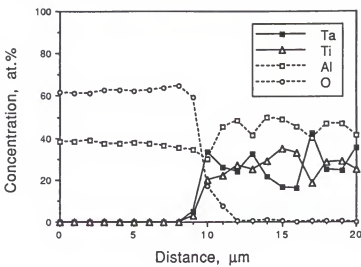
(b)

Figure 4.3 The alumina fiber/matrix interface after annealing at
1573 K for 50 h. (a) micrograph; (b) concentration
profile near the interface.

(a)

(b)
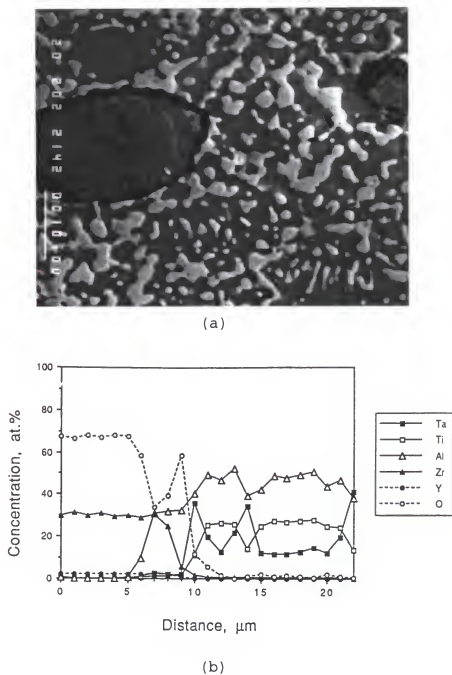
Figure 4.4 The zirconia fiber/matrix interface after annealing at
1573 K for 50 h. a) micrograph; b) concentration profile
across the interface.

Figure 4.5 The original core of a small zirconia fiber was converted to a third phase, and the dark alumina phase formed at the interface after annealing.

was around 33% but Zr concentration increased significantly. In some cases, as shown in Figure 4.5, the finer zirconia fibers from Zirca Products, Florida, New York, were completely substituted with a mixture of reaction phases and its surrounding dark band. It is not immediately evident from this study which elements were primarily responsible for production of the reaction phases. It is possible that they might have been caused by diffusion of oxygen and Zr into the matrix, or Al into the fiber. Regardless of this, the above investigation indicates that the zirconia fiber is not stable in the matrix. This finding is in contrast with the predictions based on the thermodynamic data [Stu71, Bar89] that zirconium oxide ZrO_2 should be stable with Al, Ti, and Ta at the temperature of 1573 K.

Composites Reinforced with Nitrides and Carbides

The microstructure of the zirconium nitride reinforced composite (as shown in Figure 4.6) indicated that a 3- to 10-μm-thick reaction layer was produced at the boundary region during processing and annealing. The composition profile indicated that the concentration of Zr in the interfacial zone dropped significantly and was substituted mainly by Ti and Al. The reaction product at the interfacial zone was possibly a complex nitride like $(Ti,Zr)_xAl_{1-x}N$ with a structure different from ZrN. Moreover, the depletion of Al and Ti outside the particles promoted the formation of a phase with a composition

analogous to the σ phase, which surrounded the zirconium nitride particles. Investigation on the composites with TiN particles showed instability similar to ZrN particles.

There were also distinct reaction zones at the boundary region between the matrix and carbides. An example is the extensive reaction zone near the α-SiC platelet/matrix interface. This reaction zone appeared to increase in thickness with time by consuming both the matrix and reinforcement platelets. Similar observations were made for ZrC and TiC, indicating that none of the carbides are stable in contact with the matrix alloy under the given conditions.

Composites with Other Ceramic Materials

The microstructure of the composite reinforced with titanium diboride (TiB_2) powder is shown in Figure 4.7(b). A narrow band with fine features having pointed ends, and with high concentrations of Ti and Ta, was observed around the boride particles. No attempt was made to characterize the reaction product. The thickness of the band was less than 0.5 μm after annealing, indicating that boride is possibly more stable than the investigated nitrides or carbides.

Composites with Niobium Fibers

The interfacial interaction zone of the niobium fibers in a composite annealed for 50 h at 1573 K is shown in Figure 4.8. A dark band of about 11 μm thickness can be seen between

(a)

(b)
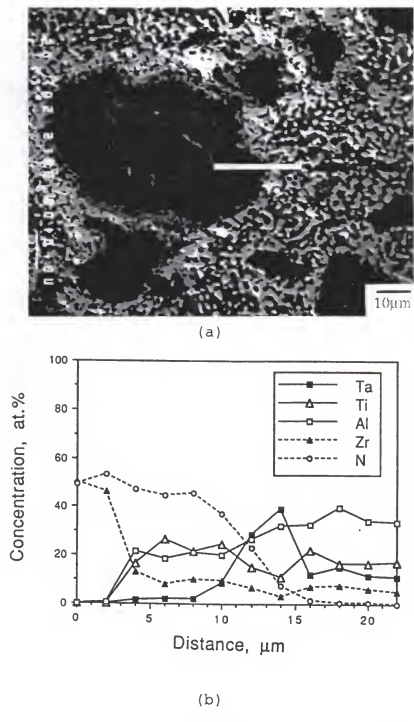
Figure 4.6 Zirconium nitride powder/matrix interface after annealing at 1573 K for 50 h.
a) micrograph; b) concentration profile.
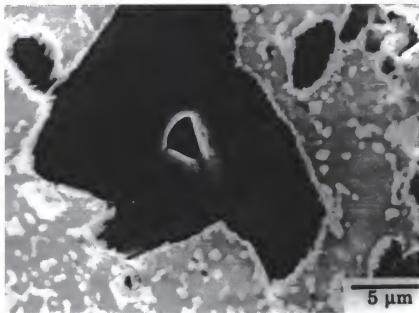
Figure 4.7 Micrograph of composite showing interfacial reaction with TiB$_2$ particle.

the niobium and matrix in the back-scattered electron image of the figure. The Al content in the band was higher than the neighboring matrix, whereas the concentration of Nb changed continuously over the region. The results indicate that niobium is not stable in contact with the matrix. As such, its use as a reinforcement for high-temperature applications for an extended period would require a diffusion barrier on the metal surface.

The feasibility of application of a diffusion barrier coating on the metal reinforcement was investigated by applying alumina coating on niobium fibers. As presented earlier, alumina was found to be stable in contact with the matrix. As described earlier in the section on "Coating on Niobium Fibers" in Chapter 3, the coating was accomplished using a sol-gel technique, which rendered a uniform and continuous alumina layer covering the niobium fibers. The composition line-scan and a micrograph of the coating in a composite are shown in Figure 4.9. The coating was uniform with a thickness of about 6 μm. As can be seen from the line-scans, the interdiffusion of constituting elements from the matrix and the metal fiber was retarded significantly by the presence of the coating. While no Nb was detected in the matrix, a relatively appreciable amount of Al was detected near the interface inside of the fiber. Nevertheless, the alumina coating on niobium fibers has significantly improved the stability of the fibers in the composite, and the alumina

(a)

(b)
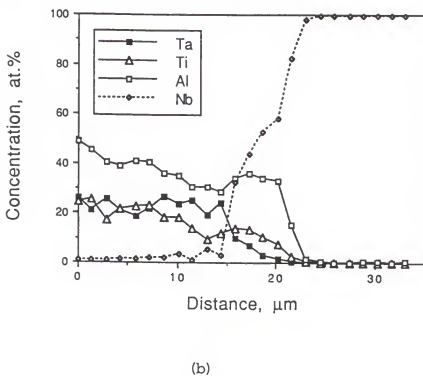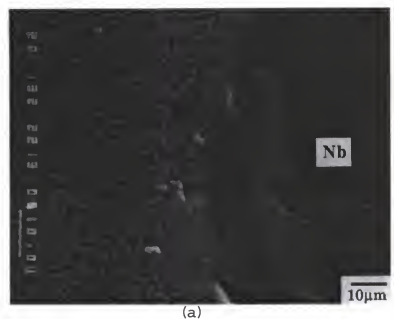
Figure 4.8 Chemical interaction between an uncoated niobium fiber
and the matrix after annealing at 1573 K for 50 h.
(a) micrograph of the composite; (b) concentration
profile near the interface.

(a)

(b)
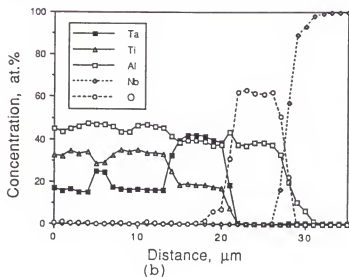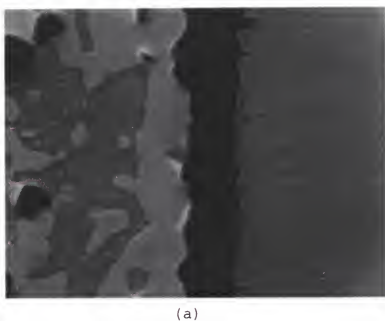
Figure 4.9 Interface between an alumina-coated niobium fiber
(right) and the matrix (left) after annealing at 1573 K
for 50 h. a) micrograph; b) composition profile across
the interface.

layer at the interface modified the mechanical properties of the interface, rendering higher toughness to the composites, as discussed later. The comparison of fracture behavior of niobium fibers with or without alumina coating showed that the coated fibers had a weaker interface, and consequently tougher composites.

Summary of Thermochemical Stabilities

The experimental study on chemical compatibility is summarized in Table 4.1. Alumina and yttria were the most stable materials in contact with the Al-25%Ti-25%Ta alloy during 50 hours of annealing in an inert atmosphere at 1573 K. Niobium was the most unstable phase among the tested reinforcement materials under the same environment. Coating of niobium with alumina significantly reduced the interaction between niobium and the matrix. Based on these results, two types of reinforcements, alumina fibers and niobium fibers coated with alumina, were selected as reinforcements for the composites.

Alumina Coating on Niobium Fibers

As discussed in the previous section, niobium was found to react with the matrix alloy at the elevated temperatures. It also was shown that coating the metal with alumina significantly reduced the chemical interaction between the reinforcement and matrix.

Table 4.1 Matrix/Reinforcement Thermochemical Stabilities

REINFORCEMENT TYPE	EXTENT OF INTERACTION	FORMATION OF REACTION PHASE
Alumina (FP fiber)	limited interdiffusion	No
Yttria	limited interdiffusion	No
Zirconia (YSZ fiber)	Extensive	Complex oxides
Zirconium nitride	Extensive	Reaction phase
Zirconium carbide	Extensive	Reaction phase
Titanium nitride	Extensive	Reaction phase
Titanium carbide	Extensive	Reaction phase
Silicon carbide	Extensive	Reaction phase
Titanium diboride	Extensive	Reaction phase
Niobium	Extensive	Reaction phase

Sol-gel coating was uniform and thick but susceptible to cracking during processing prior to hot pressing. Shaw and Abbaschian [Sha94] also found that sol-gel coating is not effective because of cracking and porosity. Therefore, for the evaluation of the mechanical properties of composites, short niobium fibers were coated with alumina through the in-situ coating process developed by Lu et al. [Lu90]. The unique process utilized conversion reaction of pre-surface-oxidized niobium to alumina during hot compaction of Al-containing alloys or compounds. The process resulted in a continuous coating in situ at the matrix-reinforcement interfaces. Lu et al. [Lu90a, Lu90b] utilized the technique for the fabrication of Nb-NbAl$_3$ composites. In this study, a similar observation was made during processing of oxidized niobium fibers and the Al-Ti-Ta matrix. It was found that a white oxide scale formed on the niobium fibers during the specified process at first. The scale on niobium was identified as a porous niobium pentoxide (Nb_2O_5), and its thickness increased parabolically with the oxidation time. The oxide layer was substituted to alumina during hot pressing of the oxidized fibers and matrix powder. Figure 4.10(a) shows that the alumina layer formed between a fiber and the matrix in the hot-pressed composite. Interrupted quenching experiments revealed that this in situ formation of alumina coating took place in a solid state conversion reaction during the consolidation of composites at

the high temperature, rather than during the early stages of hot compaction.

The thickness and morphology of the reaction products were found to depend upon the thickness of the oxide layer on the niobium. When the oxidized layer on niobium fibers was thin, isolated alumina particles formed at the interface zone after hot pressing, as shown in Figure 4.10(b). It also was observed that Nb diffused into the matrix across the original interface, which was marked by the alumina precipitates. At the same time, Al, Ti, and Ta diffused from the matrix into the niobium fibers to form a dark band of about 8-μm width inside the fibers. The concentration of Nb and Al changed abruptly at the new boundary between the band and the fiber core. It is believed that the band was an intermetallic compound phase composed mainly of Nb and Al.

When thick niobium oxide scales on the fibers were used, it converted to a complicated multi-layer zone as shown in Figure 4.10(c). Two dark bands can be seen in the figure; a thicker one in contact with the matrix and a thinner one near the niobium fiber. The dark bands were mostly alumina since their contents of Al and O were close to those in a standard Al_2O_3 sample with a little amount of Nb. Based on the observation, a possible explanation is that niobium pentoxide, Nb_2O_5, is reduced by aluminum in the matrix to produce alumina at the interface. Once an alumina layer formed, it grew toward the matrix by diffusion of oxygen and its reaction with Al
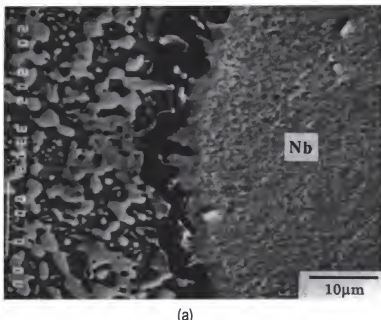
(a)

Figure 4.10   In-situ coated niobium fibers with. (a) a coating
             layer with optimum thickness showing a continuous
             alumina coating. The fiber was processed after
             preoxidation treatment at 723 K for 15 min.; (b) a thin
             coating showing interaction and diffusion between the
             fiber and matrix; and (c) a thick coating showing
             mixed oxides in the center of the coating.
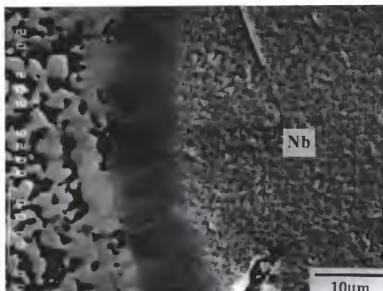
(b)
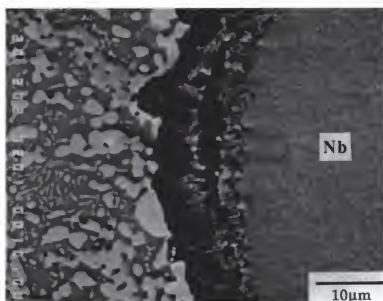
(c)

Figure 4.10-- continued

from the matrix. Evidence of this mechanism is shown in Figure 4.10(c). The boundary of the outer alumina layer had moved toward the matrix, and colonies of the two-phase matrix were taken over by the alumina layer.

The concentration distribution of Ti and Ta across the thick layer was similar to that of Figure 4.10(a), but Al and Nb contents changed differently in the multi-layer interface zone. The region between the two bands had an average composition of about 40% Nb, 35% Al, with the remainder of O, indicating that it was a mixture of niobium oxides and alumina. The concentration of niobium oxides and reduced niobium increased with temperature in the temperature range studied. The phase diagram of Al_2O_3-Nb_2O_5 suggests the formation of compounds, $Al_2O_3 \cdot xNb_2O_5$, where x is 1, 9, 25, or 49, in addition to the dissolution of some Nb_2O_5 in Al_2O_3. Thus, it is possible that the niobium oxide or niobium was dissolved at the high temperature in the alumina region, but precipitated as a mixture of oxide compounds upon cooling.

Alignment of Short Fibers

When a dry mixture of the matrix powder and short fibers without a binder or suspension media was hot pressed, the fibers in the samples were found to be randomly oriented in directions lateral to the applied pressure. Entanglement and flocculation of the fibers in the samples were also observed. In addition, there were voids between contacting fibers after

hot pressing. To eliminate the deleterious effects of these conditions on the properties of the composites, the following procedure was used to align the fibers.

The matrix powder and short fibers were mixed using a highly viscous alginate solution to disperse the fibers and the matrix powder, and also to prevent entanglement of the fibers during the alignment process. Alignment of discontinued alumina fibers and/or larger niobium fibers was achieved by forcing the suspension to a smooth convergent laminar flow through a tapered slit at a constant flow rate. During this stage, the alignment of short fibers occurred due to the velocity gradients set up between the accelerating center streamlined flow and the stationary boundary layer. The viscous drag created by these velocity gradients caused the fibers to align in the direction of motion of the suspension. The extruded tape was gelated by the immersion of the tapes in an acid bath and formation of an insoluble alginic acid. The gelated tapes were strength enough to allow their convenient handling for further processing. The tape were finally stacked to prepare green compacts.

The composites prepared by hot pressing of the stacked alginate gel tapes, in general, contained uniformly dispersed and well aligned fibers (Figure 4.11). This allowed for high loading of fibers up to at least 40% volume fraction. In addition, the technique was successfully used to prepare composites containing mixtures of FP alumina of 18.4 μm
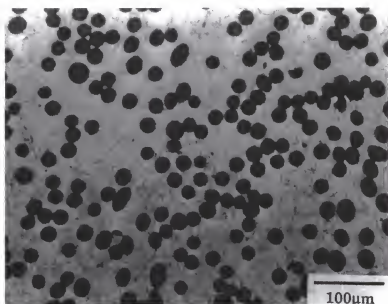
(a)
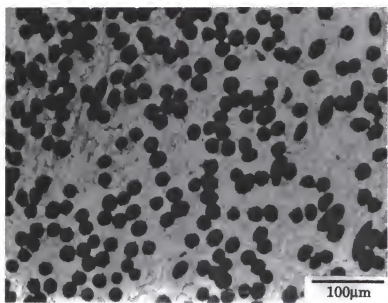
(b)

Figure 4.11 Alignment of reinforcements in composites loaded with
(a) 30 vol.%; and (b) 40vol.% alumina fibers; (c) 10
vol.% niobium; and (d) 10%/10% alumina/niobium fibers.

(c)
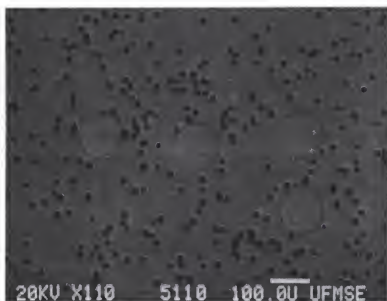
(d)

Figure 4.11 --Continued

diameter and niobium fibers of 125 μm diameter. About 40% volume fraction of the mixed fibers with high degree of alignment was attained in this study.

Some loss of fibers occurred because the reinforcements near the surface of the extruded tapes were removed while washing the tapes. For example, the measured volume fraction of the reinforcement in the composites loaded with 10, 20, 30, and 40% of FP fibers was 10, 19, 30, and 39%, respectively. The composites reinforced nominally with 10 and 20% niobium fibers contained 10 and 18% of the fibers, respectively. The hybrid composites with nominal percentage of 10%/10% and 20%/20% of alumina and niobium fibers contained 10% alumina/9% niobium and 19% alumina/18% niobium, respectively.

Due to use of the soft alginate, fiber damage was minimized during the cold extrusion process. Other researchers have reported [Alm91] severe damage to ceramic fibers in composites when a hot extrusion process was applied for alignment of short fibers. Therefore, the aligning process developed in this study is preferred for the processing of composites containing brittle fibers.

Room Temperature Mechanical Properties of Composites

Mechanical properties of the matrix alloy and its composites were measured at room temperature, and effects of the reinforcements to their mechanical properties were analyzed.

Properties of Matrix Alloy

The elastic modulus and strength of the matrix alloy were measured using a four-point flexural test at room temperature. A typical load-displacement curve of the flexural test on the Al-Ti-Ta alloy is shown in Figure 4.12. The initial non-linear region was due to the softness of testing fixtures and their adjustment at the start of the test. The curve shows the linear region representing elastic deformation up to the peak load. The maximum load was generally 10 kgf, with displacement of around 0.2 mm. The flexural strength of the alloy was estimated as 396 MPa using eq.(3.4) and the maximum load. The modulus of elasticity in bending was 226 GPa in calculation with the known load increment ΔP, and the corresponding deflection increment $\Delta \delta$ between two points in the linear region of the load-displacement curve, using eq.(3.2).

When the applied load passed the peak load, the supporting load dropped suddenly. The load-displacement curve has that commonly observed as characteristic of the behavior of a brittle material, for which the material fails catastrophically without indication of plastic deformation. That fractured surfaces developed normal to the longitudinal direction of the tested specimens also revealed brittle failure. The general view of the fracture surface of the unreinforced alloy showed rough but macroscopically flat surfaces (as shown in Figure 4.13(a)). The detailed SEM

fractograph in Figure 4.13(b) exhibits that the alloy experienced different fracture modes during testing: a mixture of intergranular and transgranular fracture. Most of the grains show cleaved surfaces, with the remainder showing grain boundary surfaces. River patterns with different directions were found on some of the cleaved surfaces of large gamma phase grains. Tilted angles of cleaved surfaces were found to be random, indicating that the crack path was deflected when it passed through the two-phase microstructure. A few of the large gamma phase grains showed river patterns parallel from grain to grain. From these observations, it can be summarized that the unreinforced matrix deformed elastically and failed in a brittle manner without any appreciable plastic deformation under bending loads at room temperature.

Fracture toughness was measured by two methods introduced in Chapter 3. From the peak load, damage tolerance of the matrix alloy was estimated as 5.59 MPa $m^{1/2}$ by applying eq.(3.10). The fracture resistance of the matrix also was estimated as the work of fracture of the matrix for comparison with those of the composites. The work of fracture was calculated using eq.(3.11) and data from the flexural tests of chevron-notched specimens at room temperature. The calculated work of fracture of the matrix was 11.7 J/m^2.
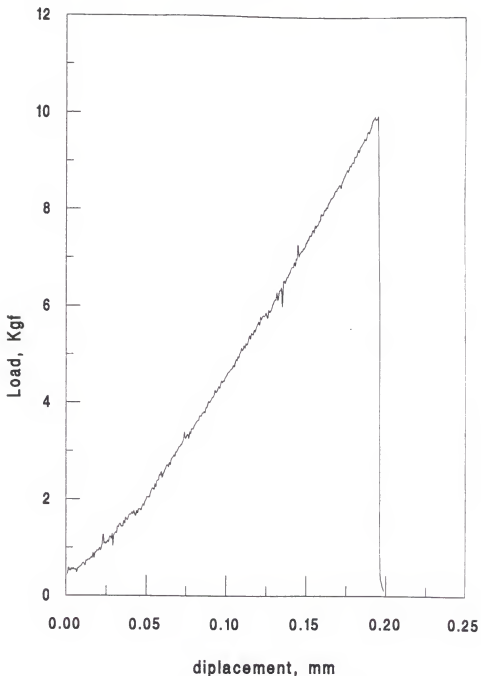
Figure 4.12 Flexural load-displacement of the matrix alloy tested at room temperature.

(a)
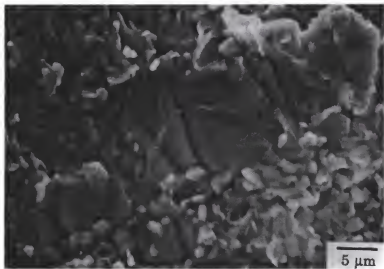
(b)

Figure 4.13 (a) Fractographs of the two-phase matrix alloy showing rough fracture surface; and (b) its detailed picture.
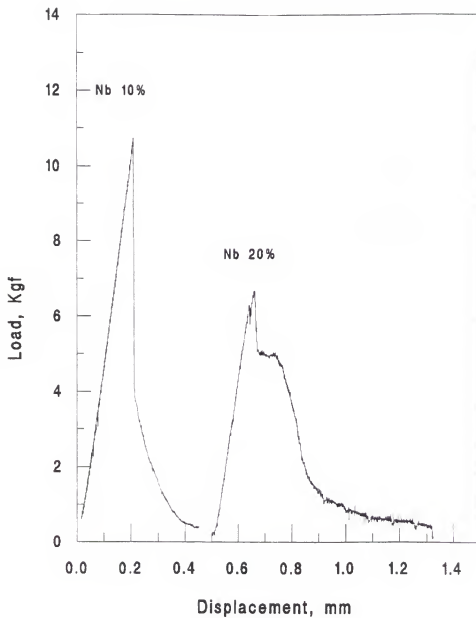
Figure 4.14   A typical load-displacement curve of room-temperature flexural test on the composites reinforced with niobium fibers.

Effect of Niobium Fiber Reinforcement

The composites failed suddenly during application of load, but unlike the matrix alloy discussed in the previous section, deflected to a larger extent than the alloy without niobium (see Figure 4.14). In addition, some stable crack propagation was achieved, as indicated by the fluctuation in the curve near the maximum load for the 20% niobium-loaded composite. After passing the peak point or the failure of the matrix during testing, the load dropped to a certain level before reaching a zero level, illustrated by the extended section of the curves in the figure. The strained metal fibers remained bridging the fractured surfaces even after the test was completed.

Toughening effect by the niobium-reinforced composites were examined by four-point bending test of chevron-notched specimens. In detail investigation of displacement-load curves in Figure 4.15 the tested composites showed a short anelastic region before reaching the peak point. The tested condition indicated reliable results because stable crack growth preceded the final unstable crack growth [Sun89]. For evaluation of toughening effect by niobium in the composites, eq.(3.10) was applied to calculate toughness of the composites. Additionally the values of work of fracture of the niobium-reinforced composites were estimated as eq.(3.11). The damage tolerance and work of fracture of the matrix and the composites at room temperature are compared in Table 4.2 and

4.3 and plotted in Figure 4.16 and 4.17. As can be seen, both the estimations of toughness of the short-fiber reinforced composites brought similar results and did not show the differences as seen in the niobium-lamellar composites of Xiao and Abbaschian [Xia92b]. As the result, large increase in toughness was achieved when the coated niobium fibers were loaded. For example, the work of fracture of the 20% niobium reinforced composite was 125% over that of the matrix alloy.

Examination of fractured surfaces of the composites reinforced with the coated niobium fibers shown in Figure 4.18(a) revealed mixed modes of failure, consisting of interface decohesion and fiber failure. A typical fiber failure under a higher magnification is shown in Figure 4.18(b). The figure shows that the niobium fiber had experienced stretching and necking after failure of the matrix, and then ruptured by void nucleation and growth. In some cases, both of the fractured specimen pieces remained bridged by some niobium fibers when load application was interrupted before complete separation of the sample.

Figure 4.18(b) shows that some debonding occurred at the fiber/matrix interface. Under detailed examination, the debonding occurred at the interface between the alumina coating and the matrix. Both debonding and extensive deformation of niobium fibers contributed appreciably to toughening due to expenditure of energy in plastic deformation of the ductile reinforcement [Eva86b, Xia91].
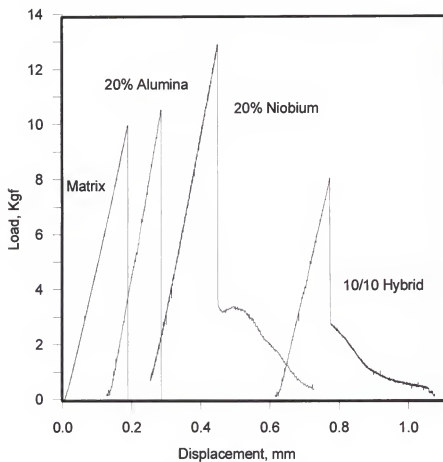
Figure 4.15 Load-deflection curves of chevron-notched bend tests.
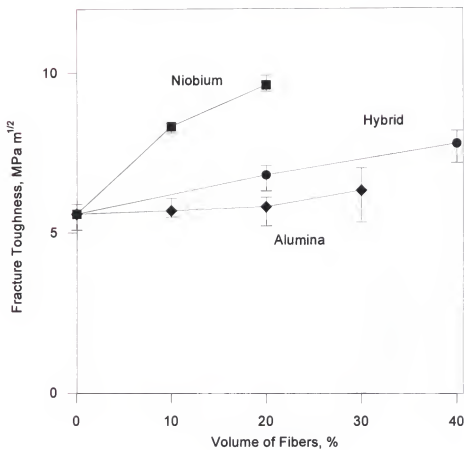
Figure 4.16 Measured damage tolerance of the composites changes with the amount of fibers in the composites.
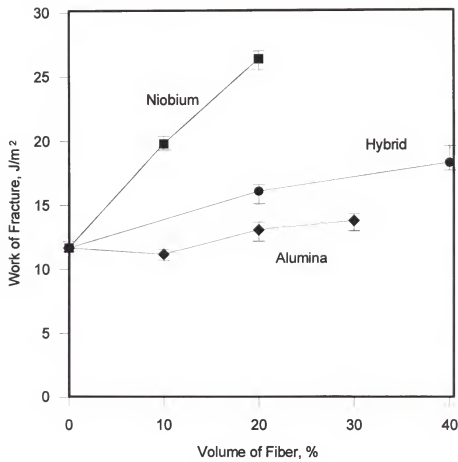
Figure 4.17 Work of fracture changes with the amount of fibers in the composites measured at room temperature by chevron-notched bend test.

Table 4.2 Damage tolerance measured at room temperature
(Unit: MPa m$^{1/2}$)

	Volume of niobium (%)	Volume of alumina (%)	Damage tolerance (MPa m$^{1/2}$)
Matrix	0	0	5.59
Niobium reinforced composites	10	0	8.32
	20	0	9.62
Alumina reinforced composites	0	10	5.69
	0	20	5.81
	0	30	6.32
Hybrid composites	10	10	6.81
	20	20	7.78

Table 4.3 Work of fracture values of the composites measured
at room temperature

	Volume of niobium (%)	Volume of alumina (%)	Work of fracture (J/m^2)
Matrix	0	0	11.7
Niobium reinforced composites	10	0	19.8
	20	0	26.4
Alumina reinforced composites	0	10	11.2
	0	20	13.1
	0	30	13.8
Hybrid composites	10	10	16.1
	20	20	18.3
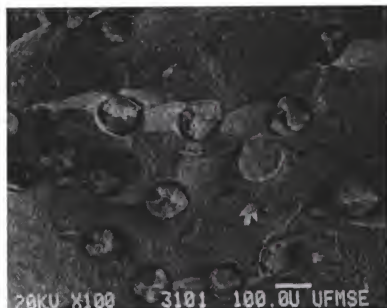
(a)

(b)

Figure 4.18 (a) Fractured composite surface with coated niobium; and
(b) its detail showing a coated niobium fiber debonded
and plastically deformed.

The unnotched specimens reinforced with the niobium fibers were also analyzed by the four-point flexural test. The resultant load-displacement curves are shown in Figure 4.14. The origin of each curve in the figure has been shifted for convenience of comparison. The initial linear portion of the curve corresponds to elastic deformation, followed by a load drop to a certain level caused by the initiation and swift propagation of a crack through the specimen. The applied load was transferred only by the bridged fibers and the material eventually failed.

The slope in the linear region was used to calculate the elastic modulus in bending according to eq.(3.2), and data of all composites are summarized in Table 4.4. These are plotted as a function of fiber volume fraction in Figure 4.19. The diagram presents that elastic modulus of the composites decreases by adding the niobium fibers with lower modulus and strength. Flexural strengths of all the composites were calculated using eq.(3.4) and summarized in Table 4.5. (see Figure 4.20).

Effect of Alumina Fiber Reinforcement

The alumina fiber reinforced composites failed in a manner similar to the matrix alloy during room temperature flexural tests. Representative load-displacement curves of the alumina-reinforced composites are shown in Figure 4.21. The curves are linear up to the peaks prior to catastrophic failure. As explained previously for the matrix and shown in
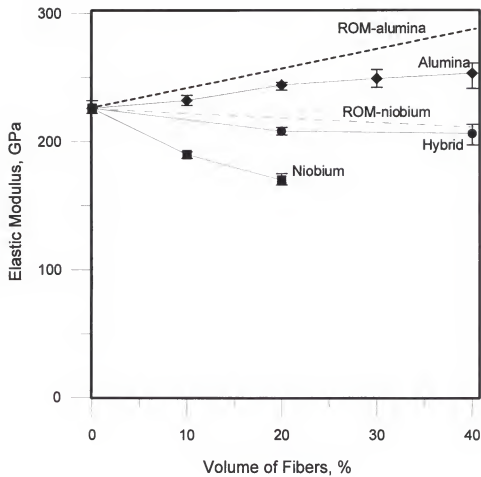
Figure 4.19   Elastic modulus in bending of the composites
at room temperature.
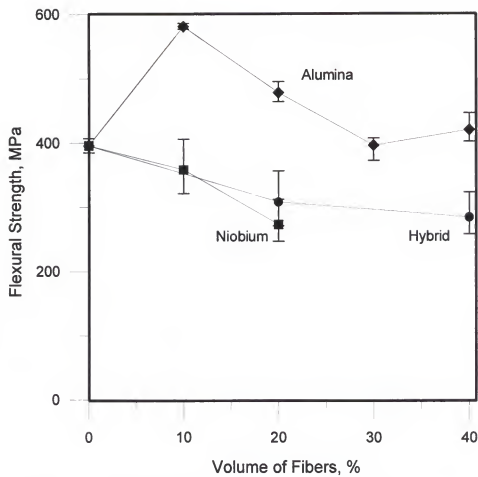
Figure 4.20 Flexural strength of the composites at room temperature.

Table 4.4 Flexural modulus of the composites at
          room temperature

	Volume of niobium (%)	Volume of alumina (%)	Measured bending modulus (GPa)
Matrix	0	0	226
Niobium reinforced composites	10	0	190
	20	0	170
Alumina reinforced composites	0	10	232
	0	20	244
	0	30	249
	0	40	253
Hybrid composites	10	10	201
	20	20	205

Table 4.5 Flexural strength of the composites at room temperature

	Volume of niobium (%)	Volume of alumina (%)	Measured flexural strength (MPa)
Matrix	0	0	396
Niobium reinforced composites	10	0	358
	20	0	273
Alumina reinforced composites	0	10	581
	0	20	478
	0	30	396
	0	40	420
Hybrid composites	10	10	308
	20	20	284

the same figure for comparison, the load drop to zero in each curve corresponds to the rapid crack propagation through the material and the failure of the specimen.

A comparison between the composites reveals that the slope of the curves increases by increasing the content of the fibers. The calculated values of elastic modulus in bending are included in Table 4.4. Strength of the specimens was calculated by eq.(3.4). Flexural strengths of the composites were obtained from the peak loads of the load-displacement curves, summarized in Table 4.5, and plotted in Figure 4.20.

Hybrid Composites

The hybrid composites containing mixtures of both of the reinforcements (alumina fibers with higher modulus and strength, and niobium fibers with lower modulus and higher toughness than those of the matrix alloy) were also tested similar to the other composites, and their properties were compared with the composites with a single kind of the reinforcements discussed previously in this chapter.

The flexural load-displacement curves obtained for composites loaded with alumina and niobium fibers are shown in Figure 4.22. The deformation behavior of the hybrid composites is similar to that of the composites reinforced only with niobium fibers. In contrast, there was a larger load drop after passing the peak load in the hybrid composites.
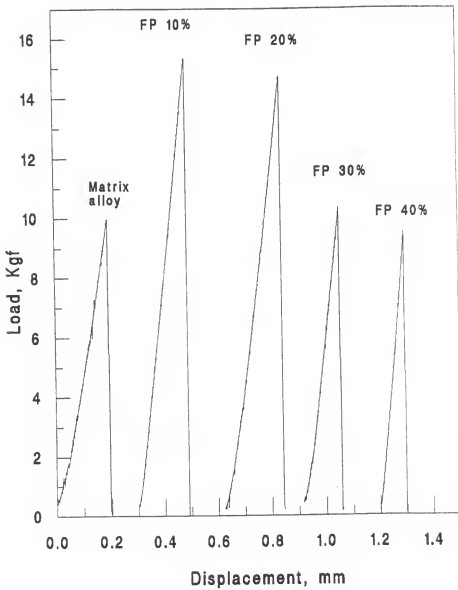
Figure 4.21 Flexural load-displacement curves of the matrix and its composites with alumina fibers obtained at room temperature.
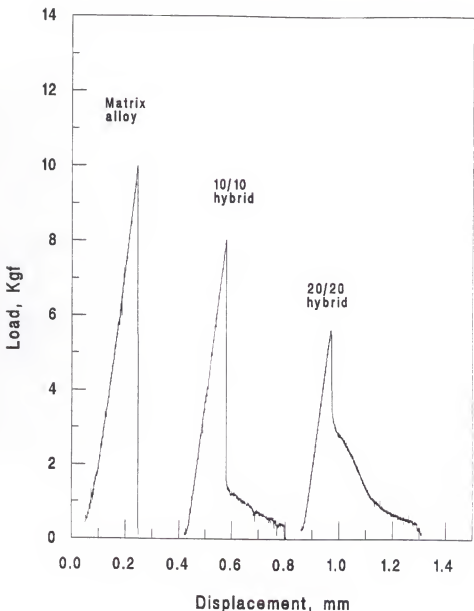
Figure 4.22 Flexural load-displacement curves of the matrix and its hybrid composites with alumina and niobium fibers obtained at room temperature.

High-Temperature Mechanical Properties of Composites

Deformation Behavior at High Temperatures

The high temperature deformation behavior of the Al-Ti-Ta alloy and its composites was measured using by four-point flexural tests at 1273 and 1473 K. The typical load-displacement curves are shown in Figures 4.23 to 4.26. In the figures, load-displacement curves of the composites with different volume fractions are compared to those of the matrix material. It should be noted that all these specimens bent to the deflection limit set by the testing fixture without failure. In order to avoid damaging the testing fixtures, the application of the load was stopped just before the bent specimens contact the testing fixture. Therefore, peak load could not be determined at the high temperatures for these samples.

The load-displacement curves of the unreinforced matrix material are linear up to proportional limit and then exhibit marked nonlinearity at 1273 and 1473 K. This behavior is characteristics of ductile material deformation; an initial elastic deformation and plastic deformation after yielding.

The composites reinforced with various amounts of the niobium and/or alumina fibers deformed plastically similar to the matrix alloy, as shown by the load-displacement curves in Figures 4.23 to 4.26. All specimens with niobium or alumina fibers were deformed plastically during testing at 1273 and
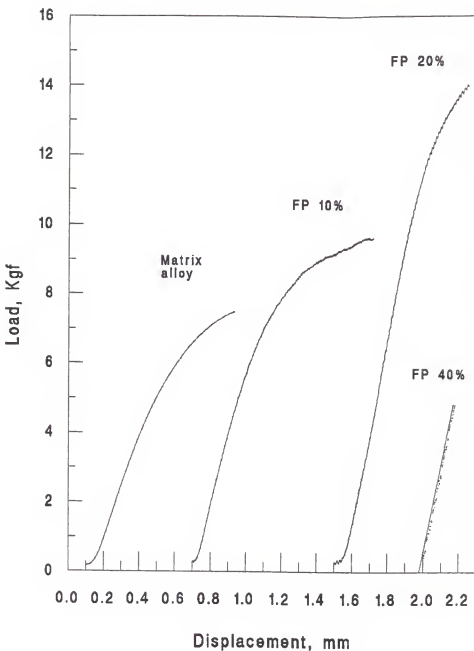
Figure 4.23 Flexural load-displacement curves of the matrix and its composites with alumina fibers obtained at 1273 K.
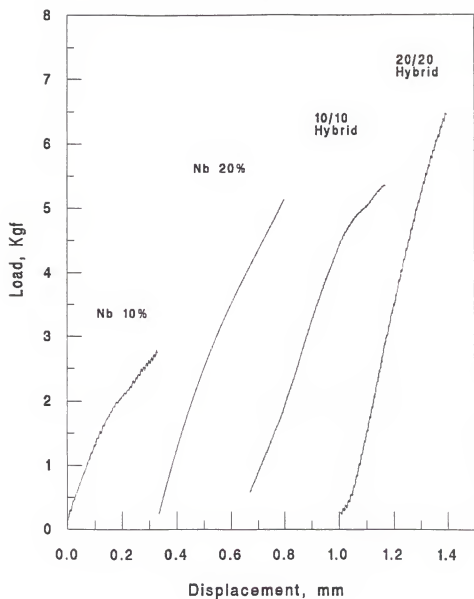
Figure 4.24 Flexural load-displacement curves of the composites reinforced with niobium fibers and hybrid composites obtained at 1273 K.
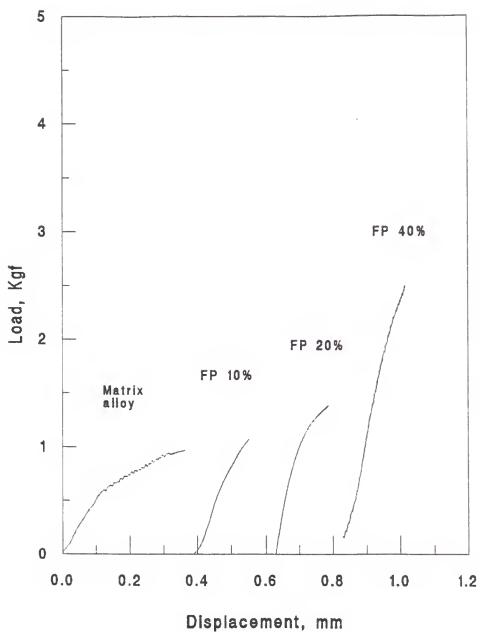
Figure 4.25 Flexural load-displacement curves of the matrix and its composites reinforced with alumina fibers at 1473 K.
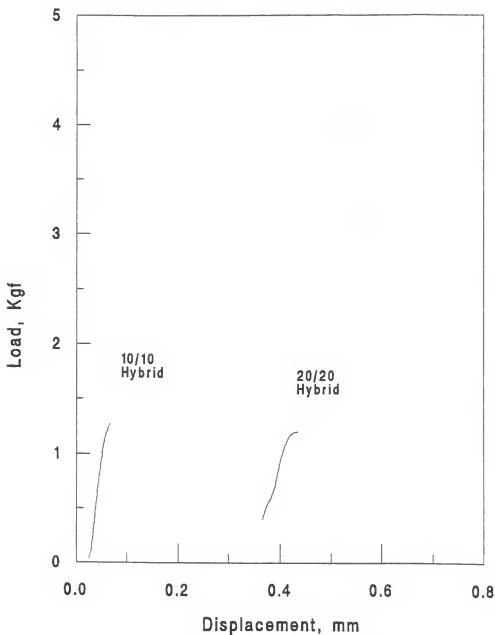
Figure 4.26 Flexural load-displacement curves of the hybrid composites obtained at 1473 K.

1473 K. The only exception is the composite containing 40% alumina fibers which was deformed elastically and failed before yielding at 1273 K. This composite failed in a brittle mode similar to the cases when the specimens were tested at room temperature. Since the matrix was ductile at the high temperature, the brittle fracture of the composite at 1273 K suggests that its fracture mechanism is different from those at room temperature.

The brittle failure of the composite is supposed by changes in the stress system starting from a more plane stress condition, that is characteristic for a ductile matrix, to a more plane strain state. The plane strain state resulted from a hindrance of constraining the matrix by addition of a large amount of the stiff fibers. Similar examples had been demonstrated in other composite systems [Fri85, Vos86].

The slope of the initially linear portion of the load-displacement curve was used to calculate the modulus of the elasticity in bending of the matrix alloy or composites. Since displacements at the high temperatures were based on measurements of only cross-head displacements, the measured quantity of $\Delta P/\Delta \delta$ was directly used to calculate the modulus by eq. (3.7). The calculated values of modulus are summarized in Table 4.6. The modulus of the alloy and composites are plotted in Figures 4.27 and 4.28. As a result of adding the alumina, niobium, or alumina/niobium fibers into the alloy, the modulus increased with the volume fraction of the fibers.
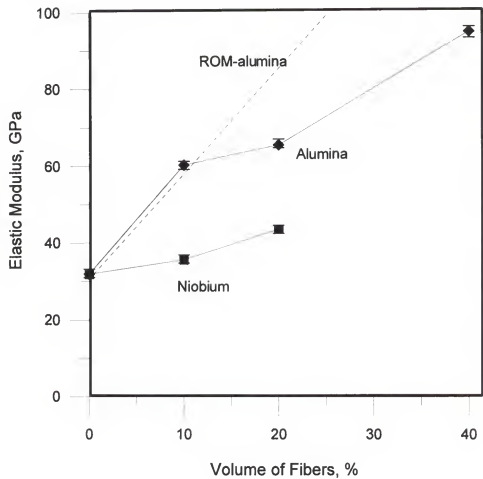
Figure 4.27 Elastic modulus in bending of the composites at 1273 K. The line represents calculated values based on the rule of mixtures.
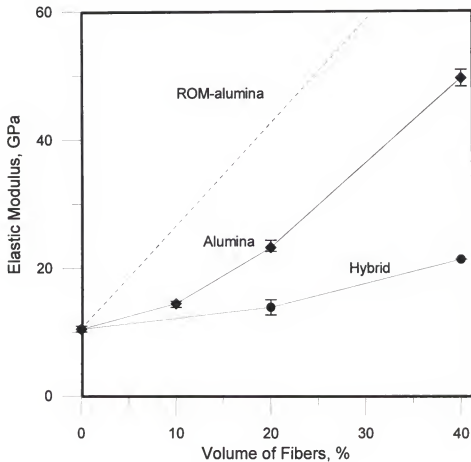
Figure 4.28 Elastic modulus in bending of the composites at 1473 K.
The line represents calculated values based on the
rule of mixtures.

Table 4.6 Bending modulus of the composites at high temperatures

Materials	Volume of niobium (%)	Volume of alumina (%)	Measured modulus (GPa)	
			at 1273 K	at 1473 K
Matrix	0	0	31.9	10.4
Niobium reinforced composites	10	0	35.6	
	20	0	43.5	
Alumina reinforced composites	0	10	60.3	14.4
	0	20	65.5	23.2
	0	40	94.8	49.5
Hybrid composites	10	20		13.8
	20	20		21.3

Among the composites, alumina fiber reinforced composites showed the most significant reinforcement effect. The modulus of the 40% alumina loaded composites is about 3 and 5 times higher than the modulus of the matrix at 1273 and 1473 K, respectively.

For calculation of flexural strength of the alloy or the composites which deformed plastically under applied loads, eq. (3.4) was used by letting P equal the applied load resulting in a permanent strain in the outer surface of 0.01%, determined by eq. (3.5). For the 40% alumina composite, on the other hand, the peak load was used as P for the calculations. More details of the data-processing procedure was described in the section on Processing of High-Temperature Deformation Data in Chapter 3 of this study. Calculated flexural strengths are summarized in Table 4.7. Flexural yield strengths at the high temperatures are compared in Figure 4.29. As can be seen, flexural yield strength of the alumina-reinforced composites increased at 1273 and 1473 K, and that of the hybrid composites increased at 1273 K. In these composites, the strength of the composites also increased with the volume fraction of the fibers. The strengthening effect of the alumina fibers was more significant at high temperatures than at room temperature. For example, the strength of the composite with 20% alumina fibers was about 2.4 times higher than that of the matrix alloy at 1273 K. The strength of the composite reinforced with 40% alumina fibers was higher than
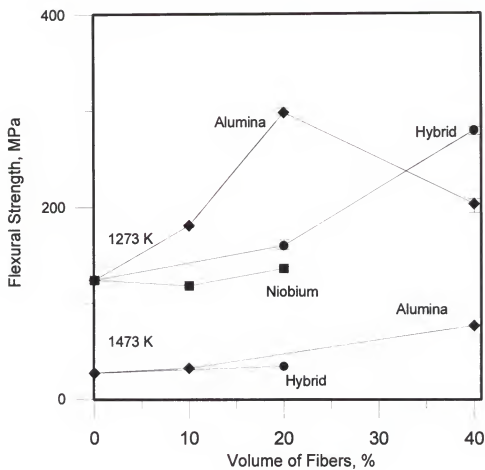
Figure 4.29 The effect of fiber loading on flexural strength of the composites tested at 1273 and 1473 K.

Table 4.7 Flexural strength of the composites at high temperatures

Materials	Volume of niobium (%)	Volume of alumina (%)	Measured strength (MPa)	
			at 1273 K	at 1473 K
Matrix	0	0	124	27
Niobium reinforced composites	10	0	118	-
	20	0	136	-
Alumina reinforced composites	0	10	181	32
	0	20	298	-
	0	40	203	76
Hybrid composites	10	20	160	34
	20	20	278	-

that of the matrix, but much lower than the projected value since it failed prematurely before reaching a yield point. In addition to the strengthening effect, the presence of the stiff fibers in the composites is believed to decrease the time-dependent deformation of the matrix material if the fibers have adequate creep resistance and are bonded to the matrix [Mcl88].

However, the strengths of the composites containing niobium fibers were close to that of the matrix material, and they showed negligible strengthening effect, although the modulus of niobium is higher than that of the matrix alloy at the high temperatures.

CHAPTER FIVE
DISCUSSION

Effect of Thermal Residual Stresses

The difference in coefficients of thermal expansion of the matrix, α_m, and of fibers, α_f, generates extreme thermal strains and residual stresses near the interface during cooling from the processing temperature. The thermal strain, ε_T developed in the composite upon cooling to the temperature, T is expressed as

$$\varepsilon_T = \int_{T_0}^{T} \Delta\alpha \, dT \qquad (5.1)$$

where $\Delta\alpha = \alpha_f - \alpha_m$, α_f and α_m being the linear thermal expansion of fiber and matrix, respectively. T_0 is stress-free temperature and T is the testing temperature. The predicted thermal strain state in the composites depends on the assumed stress-free temperature (T_0), below which thermally induced residual stresses in the matrix or fiber begin to increase with cooling. Since no experimental data of T_0 are available, it is necessary to choose a T_0 that was consistent with experimental observation of mechanical properties. Assuming various stress-free temperatures, calculation of thermal

132

Table 5.1 Thermal expansion coefficients of the matrix and
reinforcement materials [Ale89]

Temperature, ^0C	Thermal expansion coefficient (10^{-6} $^0C^{-1}$)		
	$TaTial_2$	Al_2O_3	Niobium
20	10.10	5.67	7.02
200	10.10	7.08	7.20
400	10.10	8.03	7.34
600	10.22	8.45	7.49
800	10.61	9.27	7.64
1000	11.35	10.11	7.84
1200	12.18	10.24	8.04

strains was carried out using eq.(5.1) and the thermal
expansion coefficient data in Table 5.1 [Ale89]). The
calculated thermal strains in the composites reinforced with
alumina or niobium were summarized in Table 5.2. The thermal
strain in the composites was as large as 0.250% for alumina
fibers and to 0.362% for niobium fibers when cooled from the
stress free temperature of 1473 K to room temperature. Because
α_m for both alumina and niobium is larger than α_f in the
studied composites, a radial component of the thermal stress
on the fiber was compressive upon cooling. When 20% alumina
fiber was loaded in the composite, thermal residual stress in
radial direction at the interface was estimated as 336 MPa in
compression by using eq.(2.26). Similarly, the compressive
stress of 344 MPa arose for 20% niobium-loaded composites in
compression. The estimated residual stresses were relatively
high and this will affect interfacial properties of the
composites.

The clamping stress imposed normal to the interface at
the fiber can hinder interfacial debonding and pullout of the
debonded fibers in the composites at low temperatures. The
radial pressure, σ_r, on the fibers will discourage frictional
slip between the fiber and matrix under application of an
external stress. In this case, sliding resistance is defined
by the Coulomb friction law [Mar95]

$$\tau = -\mu\sigma_r \qquad (5.2)$$

where μ is the coefficient of sliding friction between the

Table 5.2 Calculated thermal strain upon cooling from the stress-free temperature

Stress Free Temperature, K	Thermal strain, %	
	AlTiTa/alumina	AlTiTa/niobium
1473	0.250	0.362
1273	0.211	0.287
1073	0.181	0.221
873	0.152	0.162

fiber and matrix, which is considered about 0.18, as assumed from a similar system [Dev91]. Thus, when the clamping stresses occurred due to the thermally induced residual stress, the estimated maximum frictional force on the interface of alumina/matrix or niobium/matrix was about 60 MPa, that is much lower than the measured strength of the matrix and fibers.

Interfacial Strength

The above mentioned mechanical bond expected from thermomechanical clamping of the fibers by the matrix during cooling could also develop from mechanical interlocking of asperities on the fiber surface with the matrix. The experimental results indicated that the interface between the AlTiTa alloy and alumina fibers had stronger bonding. This can be seen from Figure 5.1 where all alumina fibers aligned in different directions have failed when a crack passed through the matrix and the fibers or deflected over the interface of some fibers. The fractured surfaces of the fibers were parallel, vertical, or inclined to the axial direction of each fiber. This means that the interfacial strength is large and possibly close to the fiber fracture strength. Pieces of the matrix were found attached to the surface of the alumina fibers on the fractured surface, as shown in Figure 5.2. This indicates the strong interface at room temperature was due not only to the thermal residual stress but also to a chemical
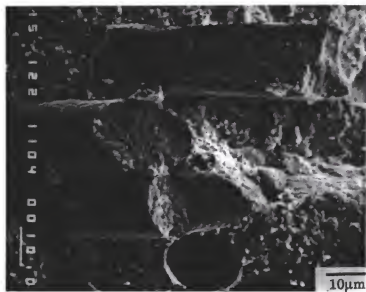
Figure 5.1   Fracture surface of an alumina fiber reinforced composite
             showing the failed matrix and alumina fibers.
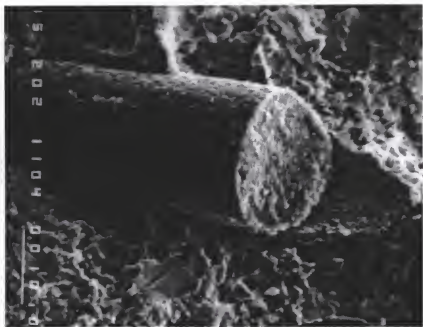
Figure 5.2.   An alumina fiber on the fractured surface showing relatively clean side surface except tiny debris of the matrix attached on the fiber.

bond between the matrix and fibers although metallography and EDS experiments detected no reaction products. The existence of a strong bond between the AlTiTa alloy and alumina is consistent with the finding of other investigations. For example, Deve and Maloney [Dev91] did not observe any debonding at Al_2O_3/AlTiTa interface. γ-TiAl is one of the two phases consisting of the Al-Ti-Ta alloy but its properties have been known more. It is known that Al_2O_3 is thermochemically stable with γ-TiAl at temperatures as high as 1773 K [Dav93]. Mackin et al. [Mac93] reported that Al_2O_3 is strongly bonded to γ-TiAl and does not debond easily during fracture.

In the composites reinforced with the coated niobium, the evidence of a moderately strong interfacial strength was observed. Figure 5.3 shows that the alumina coating fragments have adhered to the stretched niobium filaments. Cracks developed at the interface of alumina/matrix or in σ phase region near the interface (Figure 5.4). From these findings, it is proved that the interface of niobium/alumina was stronger than that of alumina/matrix.

Therefore, it is speculated that when a main crack propagated in the matrix, alumina coating or σ phase layer near the coating started to be separated from the matrix at first. Then, while the bridging niobium filament was stretching under the applied load, the adherent coating with
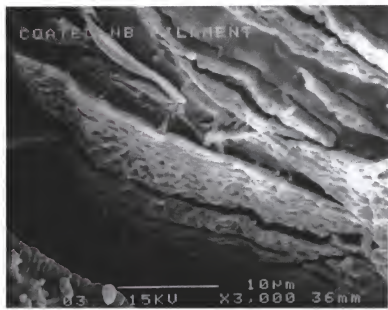
Figure 5.3   Side view of a niobium fiber debonded from the matrix and deformed.
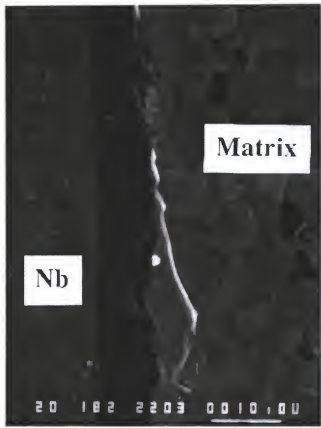
Figure 5.4   A crack passing through the matrix and the interface
              between alumina coating (dark) and the matrix.

the lower failure strain broke into fragments, which remained stuck to the filament after the filament ruptured.

Toughening by Ductile Fibers

The brittle AlTiTa alloy was toughened at room temperature by the incorporation of coated niobium fibers. In these composites, the niobium reinforcement exhibited extensive plastic deformation and debonding, before fracturing by void nucleation and growth. Figure 4.18(b) showed a debonded and fractured niobium fiber with necking and microvoids. It resembles failures of a lead fiber in a glass [Ash89] and niobium in TiAl [Cao89]. This means that the niobium fiber and matrix limited debonding and the fiber was constrained in the brittle matrix so that deformation was restricted to a small segment of the fiber.

Toughening by constrained ductile reinforcements for brittle materials has been studied by several authors [Ash89, Cao89, Sha94]. They have shown that the energy absorbed in plastic stretching of the ductile fiber provides the crucial contribution to toughness of the composite. When the interface is strong, The extent of stretching depends strongly on the degree of constraint. Extremely strong interfacial bonding would result in a high degree of geometric constraint for the ductile fibers, and crack-opening displacement corresponding to the fiber rupture would be very small which, in turn, would result in a decrease in the toughening effect. However,

optimum toughening requires weak interfaces and extensive interfacial debonding to remove the constraint and to allow fibers to neck over extensive lengths until fracture. In the presence of weak bonding at the fiber-matrix interface, higher work of fracture was obtained for continuous reinforcements [Xia92c]. On the other hand, when the fiber has a finite length, a critical minimum interfacial bond strength is required for optimum toughening. Otherwise, the fiber would be easily pulled out of the matrix before it necks, which, in turn, minimizes both the crack-surface bridging action and the toughening effect.

In this study, the toughness of the AlTiTa alloy was increased by loading niobium fibers as shown in Figure 4.17. The toughness value also increased as the volume fraction of niobium fibers increased. This relationship is comparable with eq.(2.21), which presented the effect of toughening by the constraint ductile phase. In this toughening mechanism, the volume fraction of the ductile phase is an important parameter when the other properties are invariant. Since the processing conditions were kept the same in this study, the increase in the toughness is most likely directly related to the volume fraction of the reinforcement.

Contribution of coating effect, and thus the weaker interface, was not directly connected to the toughening in this study because of a large clamping stress on the fiber by thermal residual stress in the given composites. However, the

coating prevented interfacial reaction and maintained ductility of niobium, as discussed for the results of chemical compatibility in Chapter 4. When the niobium fiber was not coated, a strong interface formed, as indicated in Figure 5.5 by the microstructure of a typical fractured surface. In the observation, the fiber showed extensive deformation which occurred only at its smaller central part because of the chemical reaction between the metal and matrix. Thus, expenditure of energy in plastic deformation was reduced and the reduced strain energy of the ductile fibers also contributed less to increase in the fracture toughness of the composite. This observation explains that uncoated metal reinforcements will contribute less to fracture toughness than coated ones.

Toughening by Alumina Fibers

Loading of the niobium fibers significantly increased the room-temperature toughness of the composites over that of the matrix alloy. However, as shown in Table 4.3 or Figure 4.17, the effect of adding the alumina fibers was modest. Due to their brittle nature, it seems that the alumina fiber and matrix failed almost simultaneously at a strain at the moment of failure of the matrix, because the measured matrix failure strain was lower than that of the alumina fiber. The fractured surface of a composite reinforced with alumina fibers, as seen in Figure 5.6, showed no mirror on the fractured surfaces of
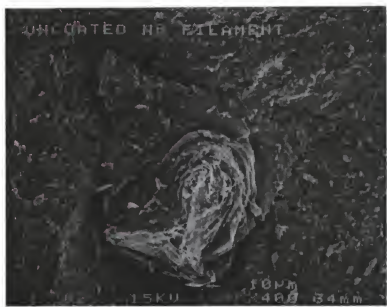
Figure 5.5 SEM micrograph of a fractured uncoated niobium fiber.
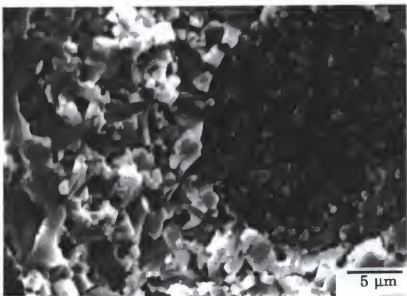
Figure 5.6 Fractograph showing a fractured alumina fiber and matrix.

fibers, indicating that the crack did not initiate from the fibers. In this type of material, one would expect that the composite toughness value is a weighted average of those of the matrix and reinforcement material according to the rule of mixtures.

As seen in Figure 5.7, the typical fracture surface of the alumina-reinforced composites is nearly flat, which indicates strong bonds formed between the fibers and the matrix. The strong bonding at the interface precluded fiber pullout as a possible toughening mechanism. A crack can be expected to deflect around a fiber if the fiber exhibits an appropriate combination of inclination to the crack plane and relative interfacial strength such as to prevent fiber fracture or fiber pullout. Thus, the toughening effect is small in absence of pullout, even with high-strength reinforcements. When brittle materials are reinforced by elastic ceramic fibers, a relatively weak interface is desirable for improving fracture toughness of the matrix in contrast to the ductile reinforcement toughening. Although the composites had a strong interface, deflection was encouraged due to residual mismatch stresses around the fiber. The local deflection varied between tilt and twist depending on the orientation. Therefore, it is believed that loading short alumina fibers into the matrix material provided minor increase in fracture toughness by crack deflection or crack shielding due to their thermal expansion mismatch.
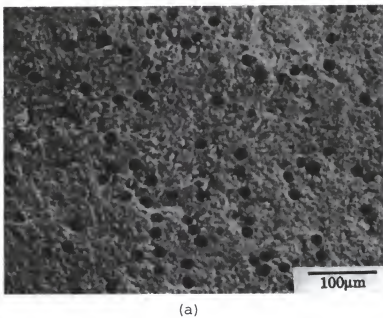
(a)
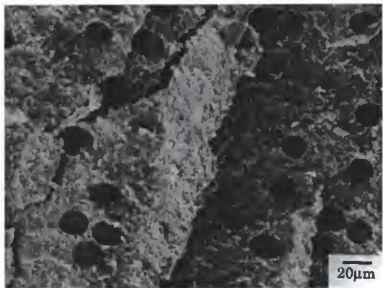
(b)

Figure 5.7 (a) fracture surface of a composite reinforced with short
alumina fibers; (b) its detail.
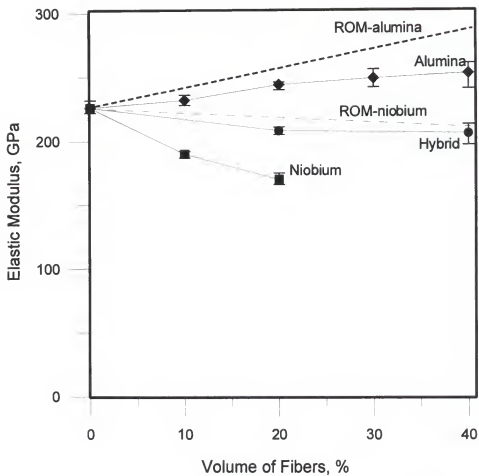
Figure 5.8   Elastic modulus in bending of composites at room temperature. The predicted values are represented by straight lines, 'ROM-alumina' for alumina reinforced composites and 'ROM-niobium' for niobium reinforced composites.

Strengthening and Stiffening at Room Temperature

The elastic modulus is a function of fiber volume fraction, as shown in Figure 5.8. For comparison, the predicted elastic modulus of the composites calculated using eq. (2.4) (see Table 5.3) also is included as a straight line in this figure. The results indicate that the elastic modulus of the composite increases by the addition of the short alumina fibers. For example, the modulus increases 12% over that of the matrix material when 40 vol.% alumina fibers were incorporated in the composite. However, discrepancies between the predicted and the measured values exist.

As discussed previously, strong interfaces existed in the composites reinforced with alumina or niobium fibers. These were induced by chemical interaction or thermally induced residual stress. When the interface between the matrix and fibers is strong, the strengthening can be predicted roughly by the rule of mixtures. The relationship between modulus and volume fraction of reinforcements was nearly linear but deviated from the rule of mixtures (ROM), which has been considered as the upper limit of composite properties [Mal88]. The deviation was due to degradation of the fiber or matrix during processing and testing, or to low loading efficiency of the discontinuous fibers.

Flexural strengths of the alumina reinforced composites are shown in Figure 4.20. The composites with 10 vol.% alumina fiber show higher values than those of the composites with

Table 5.3 Comparison between measured and predicted flexural
modulus of the composites at room temperature

	Volume of niobium (%)	Volume of alumina (%)	Measured bending modulus (GPa)	Predicted bending modulus (GPa)
Matrix	0	0	226	226
Niobium reinforced composites	10	0	190	213
	20	0	170	203
Alumina reinforced composites	0	10	232	241
	0	20	244	255
	0	30	249	272
	0	40	253	286
Hybrid composites	10	10	201	230
	20	20	205	232

higher loading of the alumina fibers. The room temperature composite strength is not much higher than that of the matrix material when fiber content is increased beyond 10%. This behavior can be explained on the basis of the microstructural homogeneity of the composite, the degree of which was likely to decrease with increasing fiber loading and, thereby, the strengthening effect of the reinforcements.

Hybrid Composite at Room Temperature

The calculated elastic moduli are plotted in Figure 5.8. The 10/10 hybrid composite contained approximately 10% alumina and 10% niobium fibers in volume, and it was expected that its properties are in an intermediate range between those of 20% alumina-reinforced and 20% niobium-reinforced composites. Properties of the 20/20 hybrid composite are between those of 40% alumina and of 40% niobium reinforced composites. As seen in Figure 5.8, elastic moduli of the hybrid composites are also approximately an average of the corresponding composites with singular reinforcement.

Toughness values of alumina, niobium-reinforced and hybrid composites are compared in Figure 4.17. The improvement in the toughness values of the 10/10 and 20/20 hybrid composites was less than those of the composites loaded only with niobium fibers, but much higher than those of alumina fiber reinforced composites.

When a single kind of reinforcement was used, all desired properties of the Al-Ti-Ta alloy were not improved at the same time. The improvement of toughness by using ductile reinforcement led to reduced stiffness. In contrast, when alumina fibers were added, the enhancement of strength and modulus was accompanied by only slight increase in toughness. These were compensated for by simultaneous addition of stiffer fibers and more ductile fibers at the same time to synthesize a hybrid composite. As a result, simultaneous enhancement in strength/modulus and also fracture toughness at room temperature was achieved by loading short alumina and niobium fibers together into the matrix alloy. Therefore, the superposition of reducing (i.e., embrittlement of the fibers, and introduction of stress concentration sites) or increasing (i.e., new energy-absorbing mechanisms, and creation of voids and crazes at fiber ends, etc.) effects improved properties of a hybrid composite.

High-Temperature Mechanical Behavior

In contrast to the brittle nature of the AlTiTa alloy at room temperature, the material deformed elastically and then plastically at 1273 K and above. In intermetallics, their dislocation systems are complicated [Alm91], and dislocations are difficult to move at ambient temperature. But the plastic deformation at such high temperatures explains that dislocation mobility became high enough to allow some plastic

deformation above the ductile-to-brittle transition temperature in the material. At such high temperatures, the presence of cracks became less important because of the plastic relaxation at sharp defects like crack tips. Therefore, the materials were deformed over the elastic limit and showed plastic deformation.

The interface strength in the composites arises from mechanical locking and compressive radial stresses that are generated during cooling. It has been a concern that bonding at the interface, hence strengthening, would be lost at high temperatures where the compressive radial stresses would be released. The calculated modulus, using the rule of mixtures and high-temperature values of the matrix and alumina or niobium fibers, was compared with the measured values. Since the ROM predictions do not significantly deviate from the measured values of modulus, it must be assumed that sufficient bonding remained at the high temperatures to allow strengthening from the fibers.

Changes in Properties at High Temperatures

Temperature dependence of elastic modulus and strength are shown in Figures 5.9 and 5.10. The composites with highest loading of fibers are included, such as 40% alumina, 20% niobium, and 20/20 dual fibers. The alumina fiber is a small-grain polycrystalline α-Al_2O_3 (FP) fiber, which retains its strength well up to 1273 K [Dhi80]. However, it exhibits
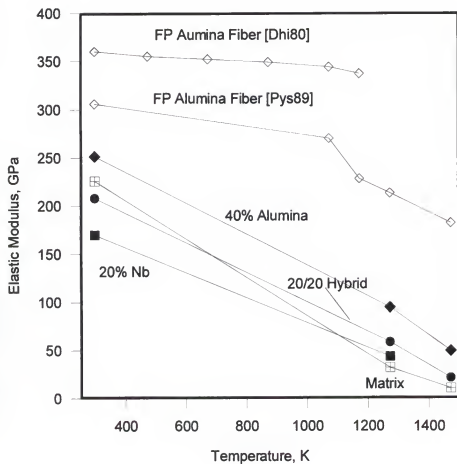
Figure 5.9   Temperature dependence of elastic modulus in bending of the matrix and composites and Young's modulus of FP alumina fiber.
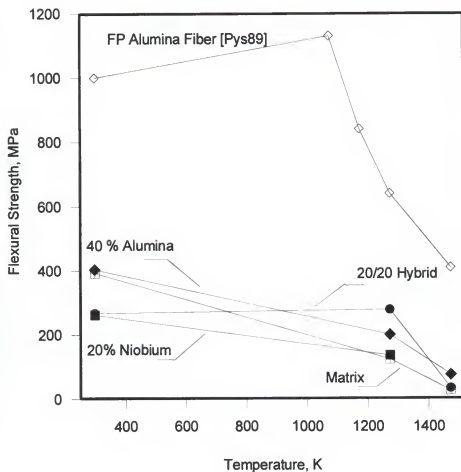
Figure 5.10 Temperature dependence of flexural strength of the matrix and composites and tensile strength of the FP alumina fiber.

grain growth and creep at temperatures above 1273 K [Pys89]. But it is known that the alumina fiber remains 64% of room-temperature strength and 70% of room-temperature modulus [Pys89]. The AlTiTa alloy weakened rapidly as testing temperature was raised above 1273 K.

At high temperatures, the composites loaded with fibers up to 40% showed the most significant effect on the modulus and strength of the composites. Changes in modulus and flexural strength of the matrix alloy and the 40% alumina-loaded composites are compared at various temperatures in Figures 5.8 and 5.9. As shown in the figures, their moduli and strengths decreased with increasing temperature. This is because matrix-dominated properties were more affected and fiber debonding and pullout occurred when temperature was raised. The strength of the composite reinforced with 40% alumina fibers was higher than that of the matrix but lower than the estimated value since it failed prematurely before reaching a yield point. At 1473 K, even the composite loaded as high as 40% FP fibers could sustain only a fraction of the load sustained at room temperature, although its strength is about 3 times higher than the matrix at 1473 K. At high temperatures, the matrix became ductile and lost most of its strength and stiffness. Stronger fiber reinforcement helped to maintain significant part of the room-temperature strength and stiffness.

CHAPTER SIX
SUMMARY AND CONCLUSIONS

Hybrid composites of Al-25at.% Ti-25at.% Ta alloy reinforced with both short alumina and niobium fibers were fabricated with improved high-temperature strength and ambient-temperature fracture toughness. To fabricate intermetallic-based composites with the desired mechanical properties, processing conditions were carefully chosen and processing parameters were optimized. Toughening and strengthening effects by the short fibers in the brittle intermetallic matrix were investigated. The main conclusions from this study are as follows:

1. High-temperature chemical stability of candidate reinforcement phases in Al-25Ti-25Ta alloy was investigated. Analysis revealed that alumina and yttria were the most stable with the matrix when annealed under an inert atmosphere for 50 h at 1573 K. However, severe reaction occurred between the matrix and other reinforcements, such as zirconia, zirconium carbide and nitride, titanium carbide and nitride, and silicon carbide. Niobium was the most unstable one among the tested materials.

2. A protective alumina coating was applied on niobium fibers by using an in-situ coating process. For this process,

158

preoxidized surface on niobium was converted to stable alumina during hot pressing of the composites. The thickness of the alumina depended upon that of the preoxidized layer, and an optimum thickness of alumina coating on niobium was obtained by controlling the extent of the pre-oxidation process. The coated niobium was found to be stable with the alloy at 1573 K.

3. Composites reinforced with short FP alumina fibers and coated niobium fibers were produced via vacuum hot-pressing process. The hot compaction was performed under 34.5 MPa applied pressure for 0.5 h at 1573 K, and mixtures of matrix powder and short fibers were fully densified to form composites.

4. The short alumina and niobium fibers were aligned unidirectionally in the composites through a cold extrusion of slurry containing the fibers and matrix powder. Uniform distribution and high loading as 40 vol.% of fibers was achieved by the alignment process.

5. The Al-Ti-Ta alloy was brittle at room temperature. The material yielded and showed plastic deformation above 1273 K.

6. Flexural strength and elastic modulus in bending of the composites were analyzed by a four-point flexural test at room temperature and at high temperatures of 1273 and 1473 K. Loading short alumina fibers enhanced stiffness of the material, but resulted in limited increase in strength.

Niobium fibers, on the other hand, caused a decrease in the elastic modulus and strength of the composites.

7. A chevron-notched bend test was performed, and work of fracture of the composites was determined. Room temperature toughness of the niobium-reinforced composites increased with volume fraction of the fibers. The toughening effect of short alumina reinforcement was neither significantly contributory nor harmful. Nevertheless, high loading of short alumina fibers increased slightly the fracture toughness of the composites. Strong bonding at interface between the matrix and alumina fiber is believed to be responsible for the small increases in toughness.

8. To analyze the combined effects of hard and ductile fibers, hybrid composites were synthesized with alumina and niobium fibers. The hybrid composites achieved simultaneous enhancement in strength/modulus and also toughness at room temperature. The property enhancement by mixing the same amount of alumina and niobium fibers resulted in an intermediate value of the individual components at room temperature.

9. At 1273 and 1473 K, alumina fibers significantly increased the elastic modulus in bending and flexural strength of the composites. The increase was proportional to the volume fraction of the fibers. The matrix and all composites deformed plastically at the high temperatures except the composite loaded with 40% of alumina fibers at 1273 K. Modulus and

strength of the hybrid composites reinforced with alumina and/or niobium increased linearly with the volume fraction of the reinforcement. There were, however, lower than those predicted by the rule of mixtures.

10. In conclusions, alumina fibers helped composites to withstand higher applied loads at high temperatures, but did not provide higher values of work of fracture at room temperature. Loading niobium into composites toughened the intermetallic at low temperature, but this also made the material fail under lower applied loads. Composites reinforced only with niobium showed lower strength and stiffness. The hybrid composites by adding stiff alumina fiber together with niobium resulted in improved properties of the intermetallic at high temperatures as well as at room temperature.

Table A.1 Properties of the matrix and reinforcements

	Matrix material	alumina fiber (FP)	Niobium fiber
Shape	powder med.dia. 15.7μm [a]	short fiber dia. 18.4 μm [b]	short fiber dia. 125 μm [d]
Composition	Al -25%Ti -24%Ta [a]	99.0% α-alumina [b]	99.8wt% niobium [d]
Melting point [K]		2317 [c]	8.66 [e]
CTE at RT [m/m K^{-1}]	10 x 10$^{-6)}$ [f]	5.7 x 10^{-6} [f]	7.0 x 10^{-6} [f]
Density [g/cc]	6.96 [a]	3.9 [b]	8.66 [e]
Tensile Strength [MPa]		1380 [c]	300 [d]
Young's modulus [GPa]	226 [a]	379 [c]	100 [e]
Elongation [%]	negligible[a]	0.4 [c]	1.44 [d]

a) measured in this work.
b) provided by the supplier.
c) [Dhi89]
d) provided by the supplier.
e) [ASM92]
f) [Ale89]

REFERENCES

Ale89   Alexander, D., Berczik, D., Bourdeau, R., Perkins, R., Svedberg, R., and Stephen, J., *Interim Technical Report P&W/GEB/FR-20756*, United Technology Corp., West Palm Beach, Florida (1989).

Alm91   Alman, D.E. and Stoloff, N.S., in *High-Temperature Ordered Intermetallic Alloys IV* eds. Johnson, L.A., Pope, D.P., and Stiegler, J.O., MRS Symp. Proc. vol. 213, Boston, Massachusetts, Nov., 1990, Materials Research Society, Pittsburgh, Pennsylvania 989 (1991).

Ash89   Ashby, M.F., Blunt, F.J., and Bannister, M., *Acta Metall.* 37 1847 (1989).

ASM92   Smithells Metals Reference Book, 7th ed., eds. Brandes, E.A., and Brook, G.B., Butterworth-Heinemann Ltd., Jordan Hill, Oxford (1992).

AST93a   ASTM Standard E 855-90, in *Annual Book of ASTM Standards*, vol.03.01, ASTM, Philadelphia 760 (1993).

AST93b   ASTM Standard D 790-92 in *Annual Book of ASTM Standards*, vol.08.01, ASTM, Philadelphia 274 (1993).

AST93c   ASTM Standard C 20-92, in *Annual Book of ASTM Standards*, vol.15.01, ASTM, Philadelphia 5 (1993).

AST93d   ASTM Standard C 1161-90, in *Annual Book of ASTM Standards*, vol.15.01, ASTM, Philadelphia 329 (1993).

AST93e   ASTM Standard C 1211-92, in <u>Annual Book of ASTM Standards</u>, vol.15.01, ASTM, Philadelphia 358 (1993).

Bar89   Barin, I., <u>Thermodynamical Data of Pure Substances</u>, VCH Verlagsgesellschaft, Weinheim, F.D.R. (1989).

Bec87   Becher, P.F., Swain, M.V. and Ferber, M.K., <u>J. Mater. Sci</u>. <u>22</u> 76 (1987).

Boe91   Boettinger, W.J., Shapiro, A.J., Cline, J.P., Gayle, F.W., Bendersky, L.A., and Biancaniello, F.S., <u>Scripta Metall. Mater</u>. <u>25</u> 1993 (1991).

Bud83   Budiansky, B., Hutchinson, J., and Lamboupolos, J., <u>Int. J. Solids Struct</u>. <u>19</u> 337 (1983).

Bud86   Budiansky, B., Hutchinson, J.W., and Evans, A.G., <u>J. Mech. Phys. Solids</u> <u>2</u> 167 (1986).

Bud88   Budiansky, B., Amazigo, J.C., and Evans, A.G., <u>J. Mech. Phys. Solids</u> <u>36</u> 167 (1988).

Cao89   Cao, H.C., Dalgleish, B.J., Deve, H.E., Elliott, C., Evans, A.G., Mehrabian, R., and Odette, R., <u>Acta Metall</u>. <u>37</u> 2969 (1989).

Cha92   Chan, K.S., <u>Met. Trans. A</u> <u>23A</u> 183 (1992).

Cla88   Clark, D.E., Dalzell, W.J., and Folz, D.C., <u>Proc. Ceram. Eng. Sci.</u>, <u>9</u>, 1014 (1988).

Cou89   Court, S.A., Loefvander, J.P.A., Stucke, M.A., Kurath, P., and Fraser, H.L., in <u>High-Temperature Ordered Intermetallic Alloys III</u>, eds. Liu, C.T., Taub, A.I., Stoloff, N.S., and Koch, C.C., MRS Symp. Proc. vol. 133, Material Research Society, Pittsburgh, Pensylvania 675 (1989).

Das91a   Das, S., and Perepezko, J.H., in Second International Conference on Light Weight Alloys for Aerospace applications, eds. Lee, E.W., Chia E.H. and Kim, N.J., TMS, Warrendale, Pennsylvania (1991).

Das91b   Das, S. and Perepezko, J.H., Scripta Metall. Mater. 25, 1193 (1991).

Dav93   Davis, J.B., Loefvander, J.P.A., Evan, A.G., Bischoff, E., and Emiliani, M.L., J. Am. Ceram. Soc. 76 1249 (1993).

Dev91   Deve, H.E. and Maloney, M.J., Acta Metall. Mater. 39 2275 (1991).

Dhi80   Dhingra, A.K., Phil. Trans. R. Soc. Lond. A294, 411 (1980).

Dot93   Doty, H., and Abbaschian, R., in Ceramic Matrix Composites and Other Systems, vol. II, Proc. Conf. Madrid, Spain, 1993, ICCM/9, 891 (1993).

Dot94   Doty, H., Abbaschian, R., and Somerday, M., in High-Temperature Silicides and Refractory Alloys, MRS Symp. Proc., Boston, MA, Nov. 1993, Materials Research Society, Pittsburgh, Pennsylvania 87 (1994).

Ebr93   Ebrahimi, F., Hoelzer, D.T., and Castillo-Gomez, J.R., Mater. Sci. Eng. A171 35 (1993).

Ebr95   Ebrahimi, F., and De Aragao, J.G., in High-Temperature Ordered Intermetallic Alloys VI eds. Horton, J.A., Baker, I., Hanada, S., Noebe, R.D., and Schwartz, D.S., MRS Symp. Proc. vol. 364, Boston, Massachusetts, Nov., 1994, Materials Research Society, Pittsburgh, Pennsylvania 1247 (1995).

Ell88   Elliott, C.K., Odette, G.R., Lucas, G.E. and
         Sheckherd, J.W., <u>High Temperature/High Performance</u>
         <u>Composites</u> MRS Proc. vol. 120 (eds.) Lemkey, F.D,
         Evans, A.G., Fishman, S.G. and Strife, J.R.,
         Materials Research Society, Pittsburgh,
         Pennsylvania 95 (1988).

Emi92   Emiliani, M.L., and Deve, H.E., <u>J. Am. Ceram. Soc</u>.
         <u>75</u> 1935 (1992).

Eva78   Evans, A.G., <u>Acta Metall</u>. <u>26</u> 1845 (1978).

Eva80   Evans, A.G. and Heuer, A.H., <u>J. Am. Ceram. Soc</u>. <u>63</u>
         241 (1980).

Eva84   Evans, A.G. and Faber, K.T., <u>J. Am. Ceram. Soc</u>. <u>67</u>
         255 (1984).

Eva86a   Evans., A.G., and Cannon, R. M., <u>Acta Metall</u>. <u>34</u>
         761 (1986).

Eva86b   Evans, A.G. and McMeeking, R.M., <u>Acta Metall</u>. <u>34</u>
         2435 (1986).

Fab83a   Faber, K.T. and Evans, A.G., <u>Acta Metall</u>. <u>31</u> 565
         (1983).

Fab83b   Faber, K.T. and Evans, A.G., <u>Acta Metall</u>. <u>31</u> 577
         (1983).

Fab83c   Faber, K.T. and Evans, A.G., <u>J. Am. Ceram. Soc</u>. <u>66</u>
         C-94 (1983).

Fle89   Fleischer, R.L., <u>High-Temperature Ordered</u>
         <u>Intermetallic Alloys III</u>, eds. Liu, C.T., Taub,
         A.I., Stoloff, N.S., and Koch, C.C., MRS Symp.
         Proc. vol. 133, MRS, Pittsburgh, PA 761 (1989).

Fri85   Friedrich, K., <u>Compos. Sci & Technol</u>. <u>22</u> 43 (1985).

Ham71   Hammant, B., _Composites_ 2 246 (1971).

Hil52   Hill R., _Proc. Phys. Soc._, A65 349 (1952).

Hoa80   Hoagland, R.G. and Embury, J.D., _J. Am. Cer. Soc._ 63, 404 (1980).

Jan91   Jansson, S., Deve, H.E., and Evans, A.G., _Metall. Trans._ 22A 2975 (1991).

Jen92   Jenkins, M.G., Ferber, M.K., Ghosh, A., Peussa, J.T., and Salem, J.A., in _Chevron-Notch Fracture Test Experience: Metals and Non-Metals_, eds. Brown, K.R. and Baratta, F.I., ASTM STP 1172, ASTM, Philadelphia, Pensylvania, 159 (1992).

JSA81   Japanese Standards Association, _Japaneses Industrial Standard JIS_ R 1601, Japan (1981).

Kel64   Kelly, A., _Proc. Roy. Soc. Lond._ A282, 63 (1964).

Kel65a   Kelly, A. and Tyson, W.R., _J. Mech. Phys. Solids_, 13, 329 (1965).

Kel65b   Kelly, A. and Davis, G.J., _Metall. Rev._ 10 1 (1965).

Kel73   Kelly, A., _Strong Solids_, 2nd ed., Oxford University Press, Oxford (1973).

Kim89   Kim, Y.S., Javed, K.R., and Abbaschian, G.J., _Final Report on Contract #N00014-86-K-0178_, Defense Advanced Research Projects Agency and the Office of Naval Research (1989).

Lan82   Lange, F.F., _J. Mater. Sci._ 17 247 (1982).

Lip85   Lipsitt, H.A., <u>High-Temperature Ordered Intermetallic Alloys</u> eds. Koch, C.C., Liu, C.T., and Stoloff, N.S., MRS Symp. Proc. vol. 39, Boston, Massachusetts, Nov., 1984, Materials Research Society, Pittsburgh, Pennsylvania 351 (1985).

Lip75   Lipsitt, H.A., Shechtman, D., and Schafrik, R.E., <u>Metall. Trans. A</u> <u>6A</u> 1991 (1975).

Lu90a   Lu, L., Kim, Y.S., Gokhale, A.B., and Abbaschian, R., <u>Intermetallic Matrix Composites</u>, ed. Anton, D.L., MRS Symp. Proc. vol. 194, Materials Research Society, Pittsburgh, Pennsylvania, 79 (1990).

Lu90b   Lu, L., Gokhale, A.B., Kaufman, M.J., and Abbaschian, R., <u>Powder Metallurgy: Key to Advanced Materials Technology</u>, ASM, Metals Park, Ohio 32 (1990).

Lu91   Lu, L., Gokhale, A.B., and Abbaschian, R., <u>Mater. Sci. Eng.</u> <u>A144</u> 11 (1991).

Mac93   Mackin, T.J., Yang, J.T., Levi, C.G., and Evans, A.G., <u>Mater. Sci. Eng.</u> <u>A161</u> 285 (1993).

Mal88   Mallick P.K., <u>Fiber-Reinforced Composites: Materials, Manufacturing, and Design</u>, Marcel Dekker, Inc., New York (1988).

Mar83   Marshall, D.B., Evans, A.G. and Drory, M.,<u>Fracture Mechanics of Ceramics</u> <u>6</u> eds. Bradt, R.C., Evans, A.G., Hasselman, D.P.H. and Lange, F.F., Plenum Press, New York 289 (1983)

Mar95   Marshall, D.B., Shaw, M.C., and Morris, W.L., <u>Acta Metall. Mater.</u> <u>43(5)</u> 2041 (1995).

Mat89   Mataga, P.A., <u>Acta Metall.</u> <u>37</u> 3349 (1989).

Mcc89   McCullough, C., Valencia, J.J., Mateos, H., Levi, C.G., and Mehrabian, R., <u>Acta Metall</u>. <u>37</u>, 1321 (1989).

Mcc91   McCullough, C., Valencia, J.J., Levi, C.G.,
         Mehrabian, R., Maloney, M., and Hecht, R., <u>Acta
         Metall. Mater</u>. <u>39</u>, 2745 (1991).

Mcd65   McDanels, D.L., Jech, R.W. and Weeton, J.W., <u>Trans.
         Metal. Soc. AIME</u>, <u>233</u>, 636 (1965).

Mcd85   McDanels, D.L., <u>Metall. Trans. A 16A</u> 1105 (1985).

Mcl88   McLean, M., <u>High-Temperature/High-Performance
         Composites</u> eds. Lemkey, F.D., Evans, A.G., Fishman,
         S.G., and Strife, J.R., MRS Symp. Proc. vol. 120,
         Materials Research Society, Pittsburgh,
         Pennsylvania, 67 (1988).

Mun80   Munz, D., Shannon, J.L., and Budsey, R.T., <u>Int. J.
         Fracture</u> <u>16</u> R137 (1980).

Mun81   Munz, D., <u>Eng. Fracture Mech</u>. <u>15</u> 231 (1981).

Mur86   Murray, J.L., <u>Binary Alloy Phase Diagrams</u>, ed.
         Massalski, T.B., ASM, Metals Park, Ohio, 173
         (1986).

New84   Newman, J.C., Jr., in <u>Chevron-Notched Specimens:
         Testing and Stress Analysis</u>, ASTM STP 855, ed.
         Underwood, J.H., Freiman, S.W., and Baratta, F.I.,
         ASTM, Philadelphia, Pennsylvania 5 (1984).

Per90   Perepezko, J.H., Chang, Y.A., Seitzman, L.E., Lin,
         J.C., Bonda, N.R., Jewett, T.J. and Mishurda, J.C.,
         <u>High Temperature Aluminides and Intermetallics</u>,
         eds. Whang, S.H., Liu, C.T., and Pope, D.P., TMS,
         Warrendale, Pensylvania, 19 (1990).

Phi86   Phillips, D.C. and Davidge, R.W., <u>Br. Ceram. Trans.
         J</u>. <u>85</u> 123 (1986).

Pre86   Prewo, K.M. and Brennan, J.J., <u>J. Mat. Sci</u>. <u>21</u> 3590
         (1986).

Pys89   Pysher, D.J., Goretta, K.C., Hodder, R.S., and
         Tressler, R.E., <u>J. Am. Ceram. Soc</u>. <u>72</u> 284 (1989).

Ram66   Raman, A., <u>Z. Metallkde</u>. <u>57</u>, 535 (1966).

Reu29   Reuss, A., <u>Z. Angew. Math. Mech</u>. <u>9</u> 49 (1929)

Rue87   Ruehle, M., Evans, A.G., Charalambides, P.G.,
         McMeeking, R.M. and Hutchinson, J.W., <u>Acta Metall</u>.
         <u>35</u>, 2701 (1987).

Sha84   Shannon, J.J. Jr., and Munz, D., in <u>Chevron-Notched
         Specimens: Testing and Stress Analysis</u>, ASTM STP
         855, ed. Underwood, J.H., Freiman, S.W., and
         Baratta, F.I., ASTM, Philadelphia, Pennsylvania 270
         (1984).

Sha94   Shaw, L. and Abbaschian, R., <u>Acta Metall. Mater.</u> <u>42</u>
         213 (1994).

Sha95   Shaw, L., Miracle, D., and Abbaschian, R., <u>Acta
         Metall. Mater.</u> <u>43</u> (1995).

Sim90   Sim, S.-M., <u>Ph.D. Dissertation</u>, University of
         Florida (1990).

Sri83   Sridharan, S. and Nowotny, H., <u>Z. Metallkde</u>. <u>74</u>,
         468 (1983).

Stu71   Stull, D.R. and Prophet, H.D., <u>JANAF Thermodynamic
         Tables</u>, 2nd ed. National Bureau of Standards,
         Publication no. NBS 37 (1971).

Sub90   Subramanian, P.R., Miracle, D.B., and Mazdiyasni,
         S., <u>Metall. Trans.</u> <u>21A</u>, 539 (1990).

Sun89   Sung, J., and Nicholson, P.S., <u>J. Am. Ceram. Soc</u>.
         <u>72</u>, 1033 (1989).

Tar81   Tarnopol'skii, Yu. M. and Kincis, T., <u>Static Test Methods for Composites</u>, trans. Lubin G., Van Nostrand Reinhold Co., New York (1985).

Tat66   Tattersall, H.G. and Tappin, G., <u>J. Mater. Sci</u>. <u>1</u> 296 (1966).

Tay89   Taya , M., and Arsenault, R.J., <u>Metal Matrix Composites: Thermomechanical Behavior</u>, Pergamon Press, Oxford, England (1989).

Tim70   Timoshenko, S.P. and Goodier, J.N., <u>Theory of Elasticity</u> 3rd ed. McGraw-Hill, New York (1970)

USD83   U.S. Department of the Army, <u>MIL-STD-1942</u> (1983).

Vir86   Virkar, A. and Matsumono, R., <u>J. Am. Ceram. Soc</u>. <u>69</u> C224 (1986).

Vos86   Voss, H., and Friedrich, K., <u>J. Mater. Sci. Lett</u>. <u>5</u> 569 (1986).

Wea91   Weaver, M.L., Guy, S.L., Stone, R.K. and Kaufman, M.J., in <u>High-Temperature Ordered Intermetallic Alloys IV</u> eds. Johnson, L.A., Pope, D.P., and Stiegler, J.O., MRS Symp. Proc. vol. 213, Boston, Massachusetts, Nov., 1990, MRS, Pittsburgh, Pennsylvania 163 (1991).

Wea92   Weaver, M.L., Guy, S.L., Falvai, M.A., Stone, R.K. and Kaufman, M.J., <u>Acta Metall. Mater</u>. (1992).

Xia90   Xiao, L., Kim, Y.S. and Abbaschian, R., <u>Intermetallic Matrix Composites</u>, ed. Anton, D.L., MRS Symp. Proc. vol.194, Materials Research Society, Pittsburgh, Pennsylvania 399 (1990).

Xia91   Xiao, L., and Abbaschian, R., <u>Advanced Metal Matrix Composites for Elevated Temperatures</u>, ASM International, 33 (1991).

Xia92a   Xiao, L., and Abbaschian, R., <u>Mater. Sci. Eng</u>. <u>A155</u> 135 (1992).

Xia92b   Xiao, L., and Abbaschian, R., <u>Metall. Trans. A</u> <u>23A</u> 2863 (1992).

BIOGRAPHICAL SKETCH

In Hwan Hwang finished his college education at Seoul National University, Korea, in 1977 and obtained his M.S. degree in materials science at Korea Advanced Institute of Science, Korea in 1979.

Hired by Daewoo Heavy Industries Ltd., Korea upon graduation, he started his career in Incheon Plant as an engineer in a special project team to establish organization systems for certification of the steel structure factory. One year later he was transferred to the new Okpo Shipyard, accompanying his divisional organization. For the next five years, he held various supervisory positions in the quality assurance, project management, and marketing technology departments.

On educational leave of absence, he entered the Department of Materials Science and Engineering, University of Florida, in 1985. After leave for working for the employer in 1992, he reentered the program in 1996.

I certify that I have read this study and that in my opinion it conforms to acceptable standards of scholarly presentation and is fully adequate, in scope and quality, as a dissertation for the degree of Doctor of Philosophy.

Reza Abbaschian, Chair
Professor of Materials
  Science and Engineering

I certify that I have read this study and that in my opinion it conforms to acceptable standards of scholarly presentation and is fully adequate, in scope and quality, as a dissertation for the degree of Doctor of Philosophy.

Robert DeHoff
Professor of Materials
  Science and Engineering

I certify that I have read this study and that in my opinion it conforms to acceptable standards of scholarly presentation and is fully adequate, in scope and quality, as a dissertation for the degree of Doctor of Philosophy.

Michael Kaufman
Professor of Materials
  Science and Engineering

I certify that I have read this study and that in my opinion it conforms to acceptable standards of scholarly presentation and is fully adequate, in scope and quality, as a dissertation for the degree of Doctor of Philosophy.

Fereshteh Ebrahimi
Associate Professor of
 Materials Science and
  Engineering

I certify that I have read this study and that in my opinion it conforms to acceptable standards of scholarly presentation and is fully adequate, in scope and quality, as a dissertation for the degree of Doctor of Philosophy.
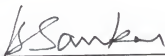
Bhavani V. Sankar
Professor of Aerospace
  Engineering, Mechanics and
  Engineering Science

This dissertation was submitted to the Graduate Faculty of the College of Engineering and to the Graduate School and was accepted as partial fulfillment of the requirements for the degree of Doctor of Philosophy.

December 1996
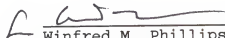
Winfred M. Phillips
Dean, College of
  Engineering

Karen A. Holbrook
Dean, Graduate School